UNIVERSITY OF CALIFORNIA

Los Angeles

Deficits in light input to the circadian system in mouse models of neurological disease

A thesis submitted in partial satisfaction of the requirements for the degree Masters of Science in Physiological Science

by

Aly Karim Mulji

2017

ABSTRACT OF THE THESIS

Deficits in light input to the circadian system

in mouse models of neurological disease

by

Aly Karim Mulji

Masters of Science in Physiological Science

University of California, Los Angeles

Professor Gene D. Block, Committee Co-Chair

Professor Christopher S. Colwell, Committee Co-Chair

Due to the cyclical nature of selective pressures in our physical world, most organisms evolved endogenous circadian timing systems that generate circadian rhythms in behavior and physiology. External stimuli such as light can reset these rhythms allowing the synchronization of the body with the external environment. Symptoms of disrupted circadian systems are comorbid with both neurodegenerative and neurodevelopmental disease states. Deficits in the ability of light information to reach the circadian system may provide a mechanistic explanation for the deregulated circadian system. Our study investigated the presence of deficits in the light input pathway to the circadian system in Huntington's Disease (HD) and Fragile X Syndrome (FXS) mouse models. We found that the ability of light information to reach the circadian system is not altered in these models and the observed circadian dysfunction may be due to an underlying pathology present in the central circadian circuit.

The thesis of Aly Karim Mulji is approved.

Cristina A. Ghiani

Ketema Nnamdi Paul

Christopher S. Colwell, Committee Co-Chair

Gene D. Block. Committee Co-Chair

Universtiy of California, Los Angeles

2017

Table of Contents **Page**

Chapter 1: Introduction and Aims

1.1 Circadian System

From an evolutionary perspective, the Earth's rotation about its axis is a fact that all organisms must adapt to in order to survive in their temporal niches. Therefore, most organisms evolved endogenous timing system with a period that is close to but not equal to 24 hours [1]. While these endogenous timing systems are present in most tissues in the body, the brain contains specific regions acting as central clocks involved in computing external stimuli and generating an appropriate output. In the mammalian brain, the hypothalamic suprachiasmatic nucleus (SCN) serves as the master pacemaker of endogenous circadian rhythms in behavior and physiology. The SCN can be synchronized to time dependent environmental stimuli also known as Zeitgebers or time givers [2]. Melanopsin-containing intrinsically photosensitive retinal ganglion cells (ipRGCs) present in the eye contain light sensitive photopigments, which can respond to and relay light information to the SCN allowing endogenous rhythms to align with the daily light and dark cycles.

1.1.2 The central circadian clock

The SCN is a network of single neuronal cell oscillators that exhibit an endogenous circadian rhythm in firing rate and clock gene expression. In both diurnal and nocturnal animals, the SCN exhibits high electrical activity during the day and low electrical activity at night [3]. The single cell oscillators of the SCN contain three core intracellular auto regulatory transcription-translation feedback loops [1]. The primary negative feedback loop involves the *Clock*, *Bmal1*, *Period1*, *Period2*, *Cryptochrome1,*

and *Cryptochrome2* genes [4] . During the day, the product of the *Clock* gene, the circadian locomotor output cycles kaput (CLOCK) protein interacts with brain and muscle ARNT-like-1 (BMAL1) to activate transcription of the *Per* and *Cry* genes by interacting with the E-box domain within the genes' promoters. The resulting PER and CRY proteins heterodimerize, translocate to the nucleus, and interact with the CLOCK-BMAL1 complex inhibiting their own transcription. Conversely, at night, the PER-CRY repressor complex is degraded allowing CLOCK-BMAL1 complex to initiate a new cycle of transcription. The secondary negative feedback loop involves retinoic acid-related orphan receptors (RORα and RORβ) as well as the nuclear hormone receptor REV-ERBα and REV-ERBβ, which are transcriptionally activated by and a direct target of CLOCK-BMAL1 complexes [5-6]. REV-ERBs repress the transcription of BMAL1, whereas RORs activate BMAL1's transcription through competition at RevDR2 and ROR binding elements (ROREs). Lastly, the third feedback loop involves the transcriptional activator D-box binding protein (DBP); yet another protein product regulated by the CLOCK-BMAL1 complex, which associates with nuclear factor interleukin 3 (NFIL3) to regulate the expression of the D-box promoter genes RORα and RORβ. Oscillating together, these three interconnected transcriptional-translational feedback loops can regulate the expression of clock genes as well as clock-controlled genes (CCG). With the discovery that clock gene oscillations are present in almost all peripheral tissues, the view of the SCN as the engine driving rhythmic changes in peripheral tissues was transformed into the concept of a central gear timing the rhythm of peripheral clocks [7-8]. Although the direct mechanisms are still being elucidated, the SCN clock can synchronize peripheral clocks through the Hypothalamic-Pituitary-

Adrenal (HPA) axis and the Autonomic Nervous System (ANS) via their respective effector hormones, glucocorticoids and catecholamines [9-10].

1.1.3 The circadian master pacemaker circuit

The appreciation that the SCN functions as the central pacemaker of circadian rhythms in physiology and behavior arose from studies in which researchers lesioned the ventral hypothamic nuclei and observed a loss of locomotor and endocrine rhythmicity [11-12]. The rhythms in locomotor activity were then re-established by grafting hypothalamic sections containing the SCN [13]. Importantly, the period of the restored rhythmic activity in the SCN-lesioned animals was that of the graft donor [14]. The ability of the SCN as a self-sustained oscillator to generate the timing and coordinate the rhythmicity of neuronal activity in other brain regions became apparent in the so-called island lesion experiments. The surgically isolated SCN still displayed persistent rhythmic neuronal activity, which was abolish in other brain regions, rhythmic prior to the lesion [15]. Furthermore, dissociated SCN neurons in culture exhibited robust circadian rhythms in electrical activity [16-17]. Therefore, it has been proposed that the coupling of individual SCN neurons combines to provide a coordinated period of electrical activity and chemical output from the SCN [18].

Traditionally the SCN has been roughly divided into a ventral (the core) and dorsal (the shell) part based on afferent input, neuropeptidergic content, and amplitude of the clock gene activity of the cells in these regions [19–21]. Generally, the core neurons receive the majority of the RHT input, exhibit low levels of activity, and express the neuropeptides vasoactive intestinal peptide (VIP) or gastrin-releasing peptide (GRP)

[22-23]. On the other hand, the shell neurons receive less input from the RHT, exhibit high amplitudes of activity, and express arginine vasopressin (AVP) or prokineticin 2 (PK2) [19], [24]. VIP and AVP are considered the primary signaling peptides of the core and shell, respectively, with the core relaying light information to the shell via VIP. Interestingly, both VIP- and AVP-containing neurons densely innervate the dorsal and ventral SubParaventricular Zone (d/vSPZ), which has been associated with regulating circadian rhythms in body temperature and sleep rhythms [21], [25]. VIP neurons project from the core of the SCN to the lateral SPZ, while AVP neurons from the shell to the medial SPZ [26].

1.1.4 The retinohypothalamic tract (RHT) transmits non-visual light information

Throughout the adaptive volatility of evolution, one of the consistent features of the physical world is the cyclical dawn and dusk of daily life, thus, light is one of the most potent Zeitgebers, able to reset rhythmic clock gene expression and the rhythms in neuronal activity within the SCN, which, in turn, relays this information to its peripheral targets. The main light receptive organ, the eye, contains various photoreceptive cells that project information to the brain. Enucleated mice still maintain endogenous circadian rhythms, but are unable to entrain to external light stimuli [27]. Visual light information is relayed to the brain through traditional rods and cones, while, non-visual light information is transduced through ipRGCs. Light sensitive cells utilize G-protein-coupled receptors (GPCRs) called opsins, which are protein moieties that are able to sense differing wavelengths of light based on their non-protein moiety, the light absorbing chromophore [28]. The framework for establishing the presence of distinct visual and non-visual light transduction pathways arose from studies demonstrating the

persistence of normal circadian rhythms and entrainment in mice lacking rods and cones [27], [29]. The identification of a human opsin, melanopsin (Opsin4, Opn4), present in cells of the inner retina restricted to the ganglionic and amacrine layers and absent in rods and cones [30], led to the discovery of ipRGCs and confirmation of their proposed projections from the eye to the SCN. This photopigment is expressed by a subset of RGCs that project to the SCN via the RHT.

Melanopsin is a GPCR using 11-*cis*-retinal as it's light absorbing chromophore, which is isomerized to all-*trans*-retinal in the presence of light causing a signal transduction cascade that results in the depolarization of the melanopsin containing cell [31-32]. 11- *cis*-retinal is maximally responsive to blue wavelengths of light [33]. Interestingly, two isoforms of functioning melanopsin have been discovered, one short (Opn4S) and one long (Opn4L) differing in the length of the C-terminal tails [34]. Through RNAi-mediated silencing studies, the functional role of the varying isoforms of melanopsin was explored [35]. In these studies, both isoforms were found to contribute to phase shifting and light mediated sleep induction. However, the Opn4S isoform was found to mediate light-induced pupillary constriction and the Opn4L isoform was associated with regulating negative masking behavior, in which mice exposed to light during their dark active phase will exhibit a complete secession of locomotor activity.

The understanding of the photic responsiveness of melanopsin-containing ipRGCs was expanded with electrophysiology studies, demonstrating that the sensitivity, spectral tuning and slow kinetics of the ipRGCs response to light matched those of the behavioral photic entrainment mechanisms [36]. Confirmation of a role for ipRGCs in photic entrainment and light response behavior came from the generation of

mice with functional rods and cones but lacking melanopsin ($Opn4^{-/-}$)[37]. Melanopsin-deficient mice were still able to entrain to light/dark (LD) cycles and their free-running period in constant darkness (DD) was not altered. Furthermore, the absence of melanopsin did not affect the normal suppression of mouse locomotor activity in the presence of light during their active dark phase, the so-called negative masking behavior. Nonetheless, $Opn4^{-/-}$ mice had attenuated phase shifting responses and a shorter period of activity rhythms in constant lighting conditions (LL) when compared to wild-type (WT) mice [37]. While the absence of melanopsin in these mice influenced some aspects of circadian entrainment, the ability of animals to entrain was still largely conserved, which highlighted the potential redundancy of the retina and the need to elucidate the presence of other players involved in this system.

The presence of potentially six morphologically distinct populations of melanopsin-containing ipRGCs (M1-M6) suggests a certain level of complexity of this system and raises the possibility for each population to be functioning differently [38]. The best characterized subtypes are the M1, M2, and M3 populations. A majority (70%) of ipRGCs contain both melanopsin isoforms and morphological analysis revealed that they were consistent with M1 and M3 ipRGC subtypes [35]. The remaining 30% of cells where shown to contain only the long isoform and were characterized morphologically as M2 cells. In relation to entrainment of circadian rhythms, M1 cells provide 80% of the retinal fiber input to the SCN, while, M2 cells make up the remaining inputs to the SCN [39]. Unlike typical RGCs, ipRGCs demonstrate intrinsic photosensitivity and do not require synaptic input from retinal photoreceptors relayed through bipolar and amacrine cells. However, synaptic tract tracing analysis of the local retinal circuit suggested that

signals from rods and/or cones might be able to modify the intrinsic light response of ipRGCs [40], [41]. Some understanding of the influence of traditional photoreceptor cells on ipRGCs came from studies on the Opn4$^{-/-}$ mice, which lack intrinsic sensitivity to light but not synaptic light input [42], [43]. In this strain, the light response of the M2 population lacking melanopsin was similar to WT animals, suggesting an involvement of the traditional photoreceptors. Conversely, the M1 cells displayed a severely attenuated response revealing the critical involvement of melanopsin in mediating their synaptic outputs. Hence, the observed ability of Opn4$^{-/-}$ mice to still entrain to light, although attenuated, could be due to the M2 population. These studies provide molecular and functional basis for the previously characterized ipRGC subtypes and may provide further insight to differential abilities of each ipRGC subtype to influence behavior.

1.1.5 Light can reset the central circadian master pacemaker

In the presence of light, ipRGCs depolarize and action potentials move along their axons within the RHT and synapse on retinorecipient cells within the SCN. The main neurotransmitters at these synapses, glutamate and pituitary adenylate cyclase-activating polypeptide (PACAP) [44], bind the NMDA and PAC1 receptor subytypes, respectively, which elicit a signal transduction cascade resulting in phosphorylatedCREB (pCREB)-induced transcription of Per1, Per2 and the immediate early gene cFos [3], and resetting of the circadian clock in the retinorecipient cells within the SCN. Recent anatomical studies characterizing the innervation pattern of a single M1 ipRGC in mouse brain showed that one M1 neuron can innervate multiple brain regions including the SCN and the vSPZ [43]. Within the SCN, these neurons

innervated distinct regions, with localized densities of retinal terminals in the ventral, medial, or dorsal portions of the SCN. Fernandez et al. (2016), showed that the recipient cells of this retinal innervation were not restricted to only VIP cells as previously thought [45]. They also reported synaptic connections of M1 ipRGCs with GRP and AVP cells as well. This expanded our understanding of the ipRGC projections to brain regions as well as provided evidence for potential redundancies present in the non-visual pathway that supplement the synaptic communication relaying light information within the SCN as well as to SCN efferent projections [43]. Interestingly, astrocytes within the SCN are among the retino-recipient cells within the SCN, which is exemplified by their ability to express the immediate early gene cFos after light exposure [46]. Along with direct light information from the RHT, the SCN receives indirect light information in the form of neuropeptide Y (NPY) projections from the intergeniculate leaflet (IGL) and serotonergic inputs from the median raphe nuclei [47], all of which serve to align the central master pacemaker and the peripheral oscillators with the daily LD cycles.

1.1.6 Deficits in the light input to the circadian system have been reported to occur in aging and neurological disorders.

Recently, reports of disrupted circadian timing systems, such as the RHT light input pathway, in neurodegenerative diseases may provide insight to the development of a desynchronized endogenous circadian rhythms [48]. Like most biological processes, rhythmic circadian timing system shows age-related changes. Aging rodents display changes in locomotor activity rhythms and slower re-entrainment following LD

cycle shifts, as well as altered light sensitivity [49]. Similarly, post-mortem studies of aged individuals reported a marked reduction in the number, density and dendritic arborization of ipRGCs [50]. A greater loss of ipRGC was reported in individuals with neurodegenerative diseases like Alzheimer's disease (AD), when compared to age-matched controls [51]. Therefore, the degeneration of ipRGC in AD patients has been implicated as a contributor to circadian dysfunction in this disease [52]. In Parkinson's disease (PD) patients, retinal nerve fiber layer thickening has been significantly correlated with PD severity and suggested as a potential biomarker of the disease [53]. Studies in Huntington's disease (HD) mouse models have shown a progressive down regulation of cone opsin and melanopsin expression in the retina [54]. Similarly, models of HD have demonstrated differential negative light masking behaviors in response to blue light pulse during their active phase as well as differential responses to blue light therapy [53]. Characterizing the integrity and functional ability of ipRGC-dependent RHT connections to SCN in neurodegenerative disease states may provide further evidence to explain the development of circadian dysfunction(s) as well as their influence on disease progression.

1.2.1 Aim 1: To determine if the BACHD and Q175 mouse models of HD exhibit deficits in the photic regulation of the SCN.

HD is a fatal neurodegenerative disease caused by a CAG repeat expansion within the first exon of the *Huntingtin* (*Htt*) gene. Translation of the mutated *Htt* results in protein misfolding, soluble aggregates, and inclusion bodies detected throughout the body [55], [56]. The presence of the mutated HTT protein leads to a dysfunction of

multiple cellular processes including, cytoskeletal organization, metabolism and transcriptional activities. Although patients primarily present with involuntary movements and loss of motor control, additionally, they present with cognitive dysfunction, affective disorders, and, importantly, sleep and circadian rhythm disruptions [57–59]. The presence of non-motor symptoms of HD can precede the onset of the disease characterized motor deficits. Circadian disruptions as well as motor deficits seen in patients have been recapitulated in animal models of the disease. Previous work from our lab has established an age- and sex-dependent progression of motor and non-motor symptoms in two mouse models of HD, the BACHD and Q175 mouse [60–62]. In both models, male mice begun to exhibit a decline in activity rhythms at 3 months old (mo), which worsen by 6mo. To counteract the progression of circadian disruptions and subsequent motor decline, we employed a blue-light enhanced therapeutic strategy [63]. While both models demonstrated improved locomotor activity rhythms and motor performance in response to blue-light therapy, still the functional recovery was attenuated in the BACHD compared to the Q175 mice. Furthermore, the BACHD mice exhibited a lack of negative masking behavior, while Q175 mice demonstrated a characteristic secession of activity in the presence of light during their active phase. Congruently, previous work has shown that the BACHD model exhibit reduced magnitude in the light-induced phase shift of the circadian system when exposed to light at CT16 [60]. This behavioral data led us to hypothesize that the BACHD model may have deficits in the light input pathway to the circadian master pacemaker. Therefore, the first aim of my thesis sought to characterize differences in the RHT light input

pathway to SCN in the BACHD and Q175 models. Therefore, I have been testing two hypotheses:

Hypothesis 1: RHT projections to the SCN are reduced in BACHD mouse, but not the Q175 mouse, compared to WT.

Hypothesis 2: BACHD mouse, but not the Q175 mouse, exhibit a decreased photic induction of cFos in the SCN compared to WT.

1.2.2 Aim 2: To determine if the *Fmr1* KO mouse model of Fragile X Syndrome (FXS) exhibits deficits in the photic regulation of the SCN.

Autism Spectrum Disorder (ASD) is a neurodevelopmental disorder characterized by deficits in social communication and well as repetitive and stereotyped interests and behaviors [64]. Patients with ASD exhibit disrupted sleep-wake patterns as well as abnormal rhythms in hormone profiles [65]. Common findings in children with ASD include dysregulation of melatonin synthesis, delayed sleep phase syndrome, rapid eye movement (REM) sleep behavior disorder, as well as comorbid anxiety, depression and epilepsy [66]. Although the aetiology of ASD and similar neurodevelopmental disorders remain elusive, there is strong evidence implicating a combination of genetic and environmental factors [67]. Fragile X Syndrome (FXS) is a X-linked inherited intellectual disability [68], which affects more severely males [69] and results from an expansion mutation of a CGG repeat sequence in the first exon of the X chromosome linked *FMR1* gene. This leads to transcriptional silencing of the gene and the gene product, the fragile X mental retardation protein (FMRP) [70]. FMRP is a selective RNA-binding protein regulating the local translation of a subset of messenger

RNAs (mRNAs) at neuronal synapses in response to metabotropic glutamate receptor (mGluR) activation [71]. Absence of FMRP results in altered synaptic function and loss of protein synthesis-dependent plasticity, leading to varying levels of neurodevelopmental and intellectual disabilities. Some behavioral symptoms presented in FXS patients as well as animal models (*Fmr1* KO) include attention deficits, autistic behaviors, aggression, anxiety, sleep disorders, and deficits in social personal skills [72]. Disruptions in rest and activity rhythms can be considered a hallmark of circadian dysregulation. Unpublished work from our lab has shown that *Fmr1* KO mice exhibit disruption in the power of locomotor activity rhythms as well as increased activity during sleep phase (Wang et al., in prep). The presence of increased activity during the light phase in these nocturnal animals points to deficits in light responsiveness. Consistent with this hypothesis, *Fmr1* KO mice, but not WT, exhibit reduced ability to entrain to a skeleton photoperiod protocol (SPP), which utilizes two short light pulses at the onset (Zeitgeber Time 0; ZT0) and offset (ZT12) of the active phase for entrainment. In addition, *Fmr1* KO mice display a loss in negative masking behavior with a 60% increase in activity in the light compared to WT mice. The presence of potential behavioral deficits in the light responsiveness of *Fmr1* KO mice could be due to deficits in the pathway of light information to the SCN. Characterizing the presence and functional ability of the RHT light input pathway to SCN in *Fmr1* KO mice may elucidate the underlying circadian dysfunction present in patients with FXS and, perhaps, other neurodevelopmental disorders, providing insight to future therapeutic strategies.

Hypothesis 1: RHT projections to the SCN are reduced in *Fmr1* KO model compared to WT

Hypothesis 2: The *Fmr1* KO model exhibits decreased photic induction of cFos in the SCN compared to WT.

Chapter 2: Materials and Methods

2.1 Animals

All experimental protocols used in this study were approved by the University of California, Los Angeles (UCLA) Animal Research Committee. Experiments followed the UCLA Division of Laboratory Animal Medicine recommendations for animal use and welfare, as well as National Institutes of Health guidelines. Every effort was made to minimize pain and discomfort.

2.1.1 Neurodegenerative models

All mutant mice used were males on the C57BL6/J background, obtained from Jackson Laboratory (Bar Harbor, Maine) in a colony managed by the CHDI Foundation, along with their littermate WT. The bacterial artificial chromosome (BAC) mouse expressing full-length human mutant HTT (BACHD mice; 4 months old, mo) employed in this study express a transgenic copy of the full length human mutant huntingtin gene encoding 97 glutamine repeats under the control of endogenous regulatory machinery [71]. The Q175 mice (6mo) arose from a spontaneous expansion of the CAG repeat in the CAG140 transgenic knock-in line [72]. These mice have been shown to have about 175 CAG repeats. We used mice heterozygous (Het) for the Q175 allele.

2.1.2 Neurodevelopmental model

Male *Fmr1* KO and WT littermate (4mo) mice on the C57BL6/J background were from our breeding colony maintained at UCLA. The *Fmr1* KO mouse was developed by Dr. Ben Oostra at the Erasmus University in the Netherlands and carries a targeted null mutation of the *FMR1* gene [73].

2.2 Anterograde tracing of the RHT

Mutant (n=3-5/genotype) and age-matched littermate WT (n=3-5, respectively) were maintained in a 12:12 LD cycle conditions. Prior to bilateral Cholera Toxin subunit B (CT-B) injections on Day 0 (**Fig.1A**), the animals received local ophthalmic anesthetic (Proparacaine Hydrochloride Opthalamic Solution 0.5%; Sandoz, Holzkirchen Germany) as well as an intraperitoneal (i.p.) injection of Carprofin, a non-steroidal anti-inflammatory drug (Zoetis, Parsippany-Troy Hills NJ). Animals were then anesthetized with isoflurane and an incision was made through sclera and into the vitreal chamber with a 30G needle (BD PrecisionGlide^{TM} Needle; Becton Dickinson, Franklin Lakes NJ); leakage of the vitreous humor out of the eye was allowed to avoid pressure build up. The anterograde tracer CT-B, conjugated to Alexa Fluor555 (2 µg in 2µl of sterile phosphate-buffered saline (PBS); Life Technologies^{TM}, Carlsbad CA) was injected bilaterally into the vitreal chamber at a 45° angle to the sclera towards the base of the retina with a 32G Hamilton needle attached to a Hamilton syringe (Hamilton, Reno NV). Five-ten seconds after the injections the needle was retracted from the eye. Animals were then assessed for recovery and placed back into their cages. Animals received a daily injection of Carprofin for 3 days. Seventy-two hours after the bilateral intravitreal injection of CT-B, mice were anesthetized with isoflurane and perfused intracardially

with PBS followed by 4% paraformaldehyde (PFA) dissolved in PBS (**Fig. 1A**). Brains were dissected out, post-fixed in 4% PFA at 4°C overnight, and then cryoprotected in 15% sucrose. Sequential coronal sections (40µm) containing the SCN were collected on a cryostat (CM3050S Leica Biosytems, Wetzlar Germany), coverslipped with Vectasheild mounting medium containing DAPI (49,6-diamidino-2-phenylindole; Vector Laboratories, Burlingame, CA), and visualized on a Zeiss Axio Imager 2 equipped with an AxioCam MRm and the ApoTome imaging system (Zeiss, Thornwood NY). Images were acquired using the Zen software (Zeiss, Thornwood NY), and a 10X objective to visualize the presence of the anterograde tracer in both the left and right SCN. The two consecutive slices containing the most central part of the SCN (mid-SCN) were carefully selected and used for all the subsequent analyses, which, unless otherwise specified, were performed using the NIH Image J software (http://imagej.nih.gov//ij). Values obtnained/genotype were utilized for group comparisons against the respective age-matching WT (WT vs. BACHD, WT vs. Q175, WT vs. *Fmr1* KO).

2.2.1 RHT tracing image analysis

After selecting and imaging two sequential sections containing the mid-SCN per animal/genotype, the position of the SCN in each image was adjusted using the transform feature of Image J to align the midpoint between left and right SCN as well as the interface between the dorsal limit of the optic chiasm and ventral limit of the SCN at the same location for each image. Regions of interest (ROI) were demarcated by eight rectangles (365µm x 136µm) arranged in a fixed 2x4 grid (730µm x 544µm) and superimposed on to each image (**Fig. 1B**). Profile plot measurements were acquired

using the profile plot feature of the Image J software, in either a horizontal or vertical conformation. The horizontal profile plot measured the average vertical column intensity, profiling the image in a horizontal direction to provide sequential average column intensity values for a given region of interest shape (**Fig. 1C**). Similarly, the vertical configuration of the profile plot measured the average horizontal column intensity, scanning the image in a vertical direction to provide average intensities of sequential rows within a given ROI (**Fig. 1D**). Using these profile conformations, the following measurements were acquired:

1) The extension of RHT fibers to the ventro-lateral region of the ventral hypothalamus were considered as the width of RHT projections. The horizontal profile analysis (**Fig. 4C**) was applied to the first two ventral rectangles (D and H) of the grid (**Fig. 4B**). These analyses provided two peaks of intensity at the lateral and medial portions of each SCN. The distances between the lateral and medial peaks were determined and considered as the width of the RHT input. Values obtained from the left and right SCN of two sequential sections/animal containing the mid-SCN were averaged and are reported as the mean ± SEM (n= 3-5 animals/genotype).

2) The extension of the RHT fibers from the optic chiasm to the dorsal SCN were considered as a measure of the height/extension of the RHT projections. We utilized a fixed ROI (730μm x 544μm; **Fig. 1D**) encompassing both the left and right SCN applying the vertical profile confirmation (**Fig. 1D**) to the ROI overlaid on to binary converted images using the default threshold parameter for the image J software. Due to the presence of minute fibers extending dorsally beyond the SCN, binary conversion of the SCN images provided an objective method to exclude these low-density fiber

values from the vertical profile. This analysis provided two peaks at the ventral and dorsal regions of the SCN (**Fig. 1E**) as well as a dorsal limit of RHT fiber densities. Using the average intensity values obtained from the vertical profile, the height of the SCN was determined as the measurement from the most ventral part of the SCN to the dorsal point in which the average intensity values of the SCN were consistently zero. Values obtained from two sequential sections/animal containing the mid-SCN were averaged and are presented as the mean ± SEM (n= 4-5 animals/genotype).

3) To quantify dorsal and ventral densities of RHT projections, average row intensity values obtained during the height measurement were plotted and presented as the vertical distance from the optic chiasm in micrometers (**Fig. 1E**). Values are presented as mean ± SEM (n= 4-5 animals/genotype).

To determine the distribution pattern of the CT-B labeled RHT fibers in the SCN, each image quantified per group was first converted into binary images using the default threshold parameter in Image J and then a 50% opacity filter was superimposed using the overlay feature of Image J. The binary images provided a measure of the presence of RHT fibers within the SCN while excluding intra-SCN differences in CT-B intensity. Overlaid images (two images per animal/3-5 animals per group) were analyzed using the interactive 3D surface plot plugin and the results are presented using the thermal look up table (Image J).

To quantify the average distribution of RHT fibers present within the SCN, the two mid-SCN images/animal were stacked in Image J, converted to binary images using the default threshold parameter, and then overlaid with 16 rectangles (183μm x 136μm) in an 8x8 grid (730μm x 544μm) (**Fig. 1D**). The average sum of pixel intensities of the

CT-B tracer within each ROI in the 8x8 grid for two images/animal/genotype were obtained using the heat map from stack plugin in Image J using the absolute parameter for calculation. The absolute parameter divides the sum of pixel intensities present in the ROI by the number of frames in the stack being analyzed. To obtain genotype specific quantification, every stacked image (2 images/3-5 animals/genotype) a heatmap from stack analysis was performed and is presented using the thermal look up table (Image J software). All the thermal lookup tables in this study utilized colors to represent the average pixel intensity, which ranged from 0 (purple) to 255 (red) for each 8-bit composite image (**Fig. 1G**).

To measure the volume of RHT fibers within the SCN of each animal, we utilized images from 14 sequential slices/animal to reconstruct the entire SCN. The position of the SCN in each image was adjusted using the transform feature of the Image J software to align the midpoint between left and right SCN as well as between the dorsal optic chiasm and ventral SCN boundaries at the same location for each image. The 14 sequential images/animal were combined into one stack using Image J as described above, and then imported into the Imaris Software (Bitplane, Zurich Switzerland) with 40 micrometer slice spacing delineated by the Imaris software for 3D reconstruction. The SCN volume was quantified using the intensity based automated surface segmentation feature of the Imaris software under the default threshold parameter (**Video 1** || **https://www.youtube.com/watch?v=j03aKk4608w**).Regions void of fluorescent signal were automatically excluded from the surface measurement, so that only those containing fluorescent signal were automatically reconstructed. Values for both the left

and right SCN of each animal were averaged and are shown as mean ± SEM (n= 4-5 animals/genotype).

Fig.1

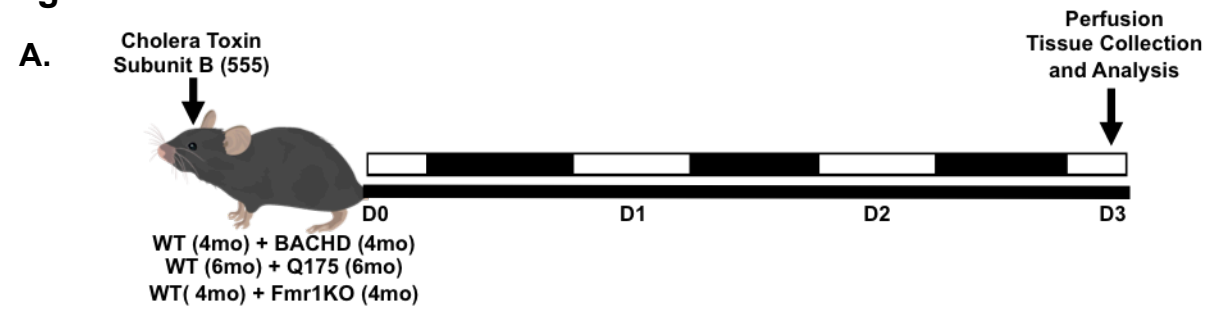
A.
Cholera Toxin
Subunit B (555)
Perfusion
Tissue Collection
and Analysis
D0
D1
D2
D3
WT (4mo) + BACHD (4mo)
WT (6mo) + Q175 (6mo)
WT(4mo) + Fmr1KO (4mo)

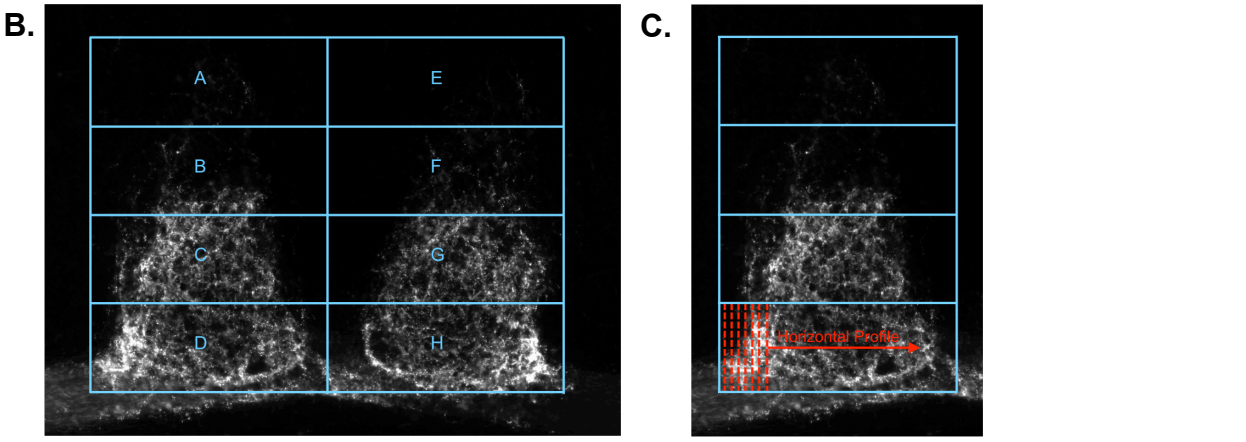
B.
A
E
B
F
C
G
D
H
C.
Horizontal Profile

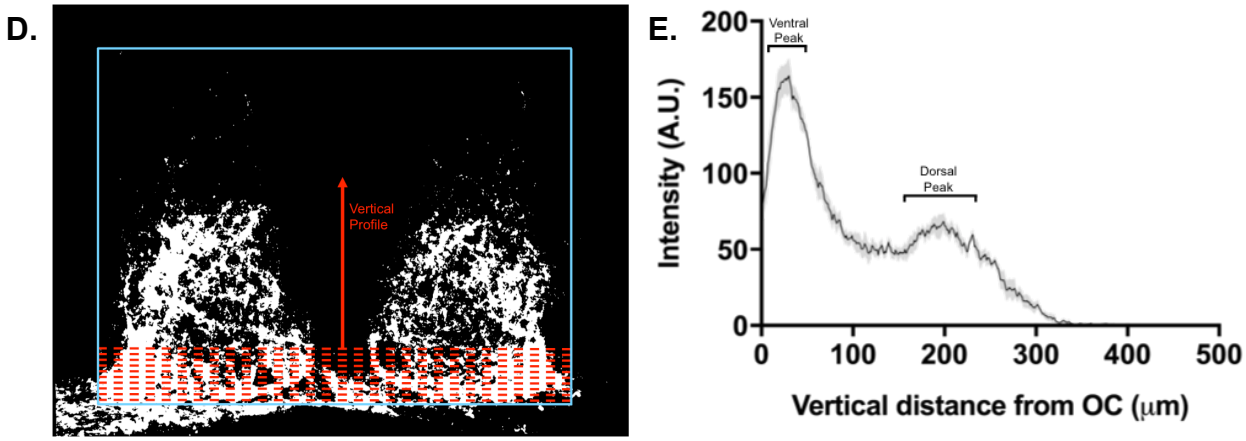
D.
Vertical
Profile
E.
Ventral
Peak
Dorsal
Peak
Intensity (A.U.)
200
150
100
50
0
0
100
200
300
400
500
Vertical distance from OC (μm)

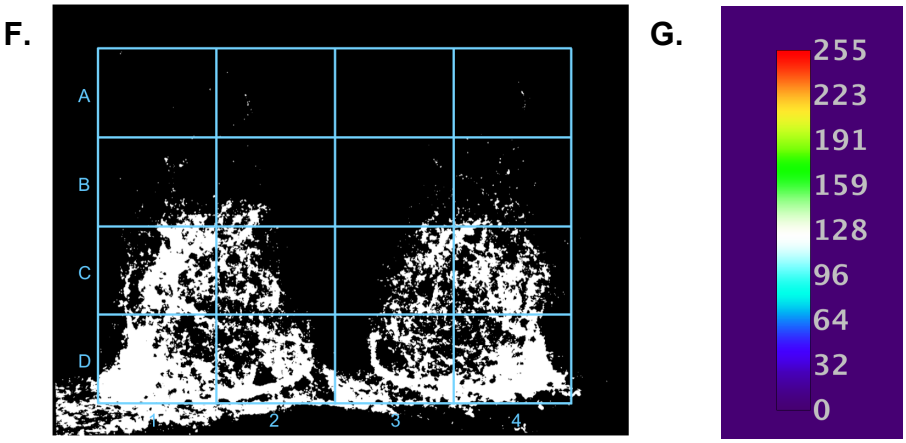
F.
A
B
C
D
2
3
4
G.
255
223
191
159
128
96
64
32
0

Fig. 1: RHT tracing experimental design, timeline, and analysis methods. (A) Anterograde RHT tracing experiment. Age-matched WT and mutant mice received bilateral intravitreal injections of the fluorescent tracer, Cholera Toxin Subunit B (CT-B), on Day 0 (D0). After the injections, the animals were placed back in standard lighting conditions (12:12 LD). Animals were perfused and the tissue collected for analysis 72 hours later (D3). **(B)** Representative RHT tracing experimental image overlaid with a fixed 2x4 analysis grid (730µm x 544µm) dorso-ventral extension of CT-B labeled RHT projections to the SCN. **(C,D)** Schematics of the profile plot analyses conducted in the horizontal or vertical configuration to determine medio-lateral or ventro-dorsal extension respectively. **(E)** Representative plot obtained from vertical profile of region of interest (ROI;730µm x 544µm) overlaid on to binary images to assess the ventro-dorsal densities of RHT fibers. **(F)** Representative binary image with a fixed 8x8 analysis grid (730µm x 544µm) overlay utilized to determine the distribution pattern of RHT projections within the SCN. **(G)** Thermal pseudo-color legend with representative 8-bit pixel values (0-255).

2.3 Photic induction of cFos

WT (n=4) as well as age-matched mutants (n=3-5) were individually housed in DD conditions with access to a running wheel for three days (day 0 to day 3, **Fig. 2A**). Locomotor activity for each mouse was recorded using infrared sensors and analyzed using the El Temps (A. Diez-Nogura, Barcelona, Spain; http://www.el-temps.com/principal.html) and Clock Lab programs (Actimetrics, Wilmette, IL) to determine free running activity. WT and mutant mice were exposed to white light (50 lux for 10 min) at circadian time (CT) 16 (4 circadian hrs after activity onset). By definition, CT 12 is the time when nocturnal animals begin their daily activity. Sixty min after light exposure, mice were anesthetized with isoflurane and perfused intracardially and the brain collected as reported above. Sequential coronal sections (50 μm) containing the entire SCN were collected. Immunolabelling of frozen sections was performed as previously described [73], [53]. Briefly, sections were blocked in carrier solution (1% BSA and 0.3% Triton X-100) containing 10% normal donkey serum for 1 hr at RT and, then, incubated overnight at 4^{o}C with primary antibodies against cFos (rabbit polyclonal 1:500, EMD Millipore, Temecula, CA) diluted in carrier solution containing 5% normal donkey serum, followed by the appropriate secondary antibody conjugated to Cy3 (Jackson ImmunoResearch Laboratories, West Grove, PA). Immunostained sections were mounted in Vectashield mounting medium with DAPI (49,6-diamidino-2-phenylindole; Vector Laboratories, Burlingame, CA), and visualized on a Zeiss Axio Imager 2 equipped with an AxioCam MRm and the ApoTome imaging system (Zeiss, Thornwood NY).

2.3.1 Photic induction of cFos image acquisition and analysis

Z-stack images (15 slices, 10µm Z-depth) were acquired with a 40X objective using the Zen software (Zeiss, Thornwood NY), and the SCN borders identified and traced using the Axiovision software and the DAPI staining as reference (Zeiss, Thornwood NY). All the cFos positive cells were counted in three consecutive sections at the level of the mid-SCN/animal with the aid of the cell counter plugin of the Image J software by two observers masked to the genotype and experimental conditions. Values from the left and right SCN were averaged.

The three consecutive images/animal, were then used to measure the mean intensity of cFos staining in a ROI (348µm x 466µm; **Fig. 2B**) containing either the left or right SCN using Image J. The distribution of cFos immunoreactivity throughout the SCN was analyzed using the horizontal or the vertical profile plot configuration in Image J (**Fig. 2B**-**C**) for the given region of interest. The values generated from the profile plot analysis were imported to excel and a best-fit 6^{th} order polynomial line was applied and used for data alignment. Sequential average column intensity values obtained from each image were adjusted in the horizontal or vertical direction to align the peak of average intensity for each image. To visualize the distribution of cFos immunoreactivity with respect to the SCN, heat maps from stack analysis was performed on the same image data set used for counting and profile plot analysis. Using a non-specific nuclear marker (DAPI), SCNs located to the right of the third ventricle were flipped horizontally and the ventral and medial limit of both left and right SCN were aligned to be present at the same location in each image. The aligned images were then separated into stacked images (6 images/animal) with respect to genotype, treatment (light exposure or no light

exposure) and fluorescent signal (cFos or DAPI). The purpose of this analysis was to observe any region specific differences in cell immunoreactive for cFos and not to analyze differences in levels of immunoreactivity among cFos expressing cells within the SCN. Therefore, in order to exclude differences in intensity resulting from varying levels of cFos expression in cells within SCN, each image stack was converted to binary using the mean threshold parameter of the Image J software. Binary stacks were then submitted to heat map analysis with an 8x8 ROI grid (380μm x 445μm; **Fig. 2D**). It is important to note that this is a novel method of analysis and without further validation the results from this analysis can only be considered preliminary.

2.6 Statistical Methods

Data were analyzed using the GraphPad Prism 7 software (GraphPad Software, La Jolla, CA) using the Student's *t*-test. Two group comparisons were between age-matched WT animals and mutant animals (BACHD, Q175, or *Fmr1* KO). All Results are shown as the mean ± SEM.

Fig.2

A.

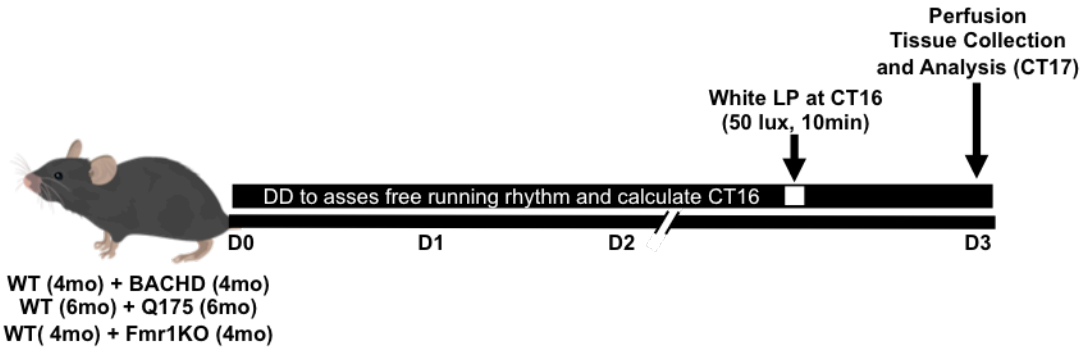
Perfusion
Tissue Collection
and Analysis (CT17)
White LP at CT16
(50 lux, 10min)
DD to asses free running rhythm and calculate CT16
D0
D1
D2
D3
WT (4mo) + BACHD (4mo)
WT (6mo) + Q175 (6mo)
WT(4mo) + Fmr1KO (4mo)

B.

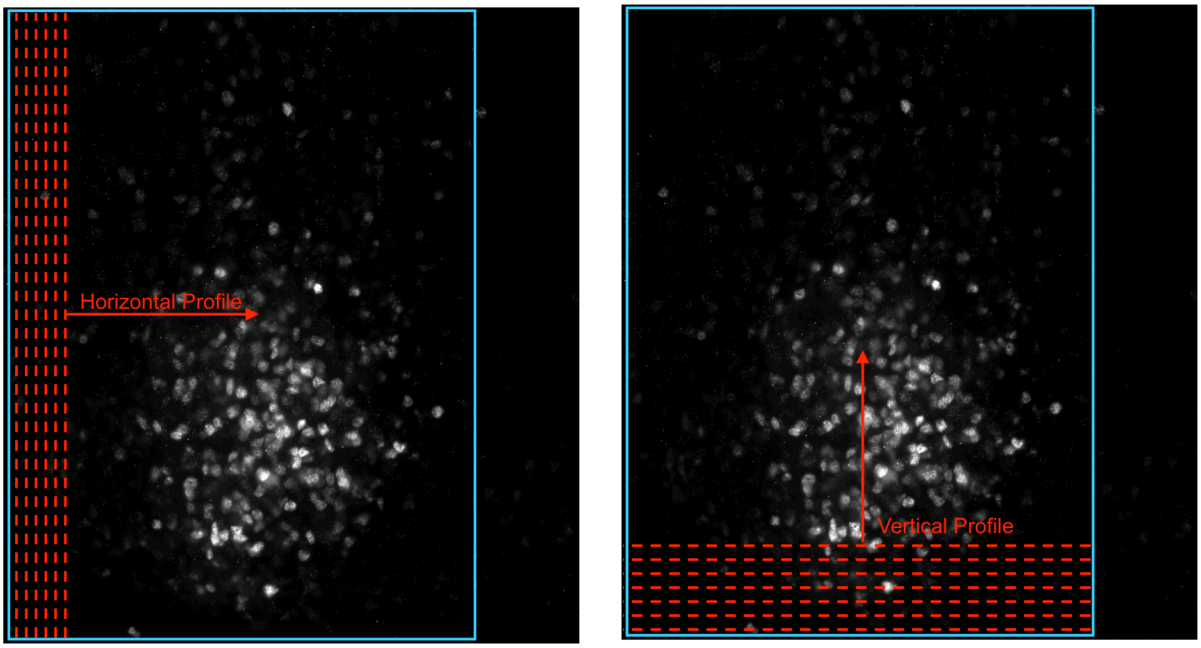
Horizontal Profile
Vertical Profile

D.

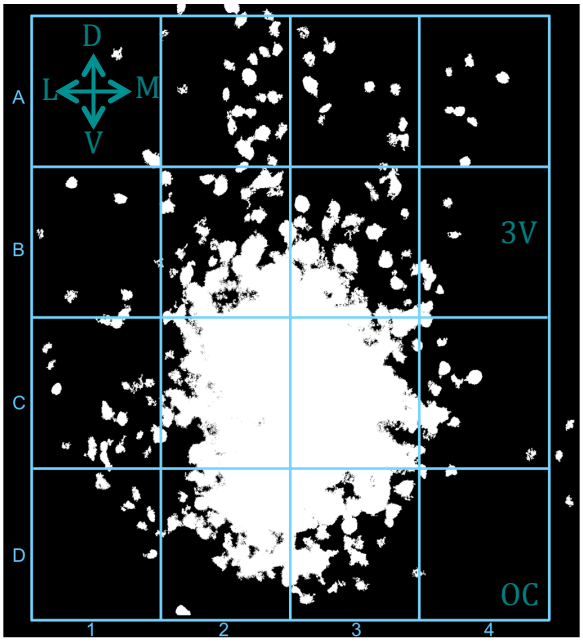
D
L
M
V
A
B
C
D
3V
OC
1
2
3
4

Fig. 2: Light-induced cFos expression experimental design, timeline, and analysis method. (A) Timeline of light induction of cFos in retino-recipient cells in the SCN. Age-matched WT and mutant mice were placed in constant darkness conditions (DD) on D0 to assess free running behavior and calculate their circadian time 16 (CT16). On D3 mice received one 10min white light pulse (LP) at CT16 and were sacrificed for tissue collection and analysis one hour after the start of the LP. **(B,C)** Representative high magnification image of light-induced cFos expression overlaid with a fixed region of interest (348μm x 466μm) and schematic of the horizontal or vertical profile plot analysis used to determine distribution of cFos positive cells within the SCN. **(D)** Representative high magnification binary image of light-induced cFos expression overlaid with a fixed 8x8 analysis grid (380μm x 445μm) utilized to quantify distribution.

Chapter 3: Is the light input to the SCN intact in mouse models of HD?

3.1 Introduction

The mechanism by which external light information entrains the mouse circadian rhythms in behavior and physiology is dependent on the intrinsic connections from the eye to the SCN via the RHT. IpRGCs in the eye respond to light and their axons relay non-visual light information by traveling along with the optic nerves and exiting at the level of the optic chiasm to innervate the SCN. This light information will reset circadian clocks in the brain as well as in peripheral tissue, which will coordinate daily changes in physiology and behavior allowing the appropriate adaptation to an animal's environment. Disconnection between the external environment and the internal circadian system can allow development of circadian dysfunctions, which may potentially influence the disease progression in genetically predisposed individuals. HD patients exhibit sleep disorders, which may correlate with lower cognitive and functional performance [74]. Congruently, mouse models of HD exhibit similar disruptions in circadian rest/activity cycles [59; 61; 75]. Recent work from our lab has shown that HD mouse models display deficits in behavioral light response [63]. Characterization of any deficits in the light input pathway to the circadian system in these models can provide insight for potential therapeutic strategies to delay the progression of HD symptoms.

3.2 Analysis of RHT input to the SCN of BACHD mice.

Deficits in the RHT connections to the SCN can disrupt mechanisms of entrainment allowing the persistence of deregulated circadian rhythms, which can be considered a mechanism that can exacerbate disease symptoms. To assess the

integrity of the RHT projections in HD, we employed bilateral intravitreal injections of the anterograde tracer CT-B in the HD mouse model named BACHD and age-matching WT mice. Both WT and BACHD mice showed elaborate RHT projections to sections of the mid-SCN (**Fig. 3A**). In general, the retinal input showed the expected dense RHT fibers populating the ventral region of the SCN in both genotypes, while sparser fibers were seen in the center of the nuclei [76]. However, upon careful examination, we observed subtle abnormalities in the RHT pathway in middle SCN sections of BACHD mice. These mutants displayed a small non-significant reduction (WT: 201±5μm; BACHD: 189±5μm; t=1.73, p=0.13) in the projections of the RHT fibers that extend medio-laterally (width) in the ventral hypothalamus (**Fig. 3B**), and a insignificant increase (WT: 440±8μm; BACHD: 467±22μm; t=1.21, p=0.29) in the height (ventro-dorsal) of the fibers extending towards the dorsal hypothalamus as compared to WT (**Fig. 3C**). The CT-B signal could still be detected beyond the dorsal region of the SCN (**Fig. 3A**). There was no significant difference in the volume of RHT projections within the SCN of BACHD ($1.5x10^7$±$8.7x10^5$μm^3) mice when compared WT mice ($1.5x10^7$±$9.2x10^5$μm^3; t=0.055, p=0.96; **Fig. 3D**). Within the SCN, WT animal exhibited a greater distribution of ventral projecting RHT fibers, while BACHD mice exhibited a slight increase in the extension of dorsal density of RHT fibers in the SCN (**Fig. 3E**).

To better assess the RHT fiber distribution (**Fig. 4A**), we quantified the presence of the CT-B signal using overlaid binary images superimposed with ROI within the SCN (**Fig 4B**). WT animals exhibited a greater presence of fibers in the ventro-lateral regions of the SCN (**Table 1**; ROI: 1B, 1C, 1D, 4B, 4C, 4D), while the BACHD mice showed a higher presence of RHT fiber in the dorso-medial regions of the SCN (**Table 1**; ROI: 2B,

2C, 2D, 3B, 3C, 3D). Although the overall distribution of the RHT fibers to the ventral hypothalamus of BACHD mice was maintained, these results suggest that the BACHD model exhibits subtle differences in the pattern of terminal RHT fibers within the SCN.

Fig. 3

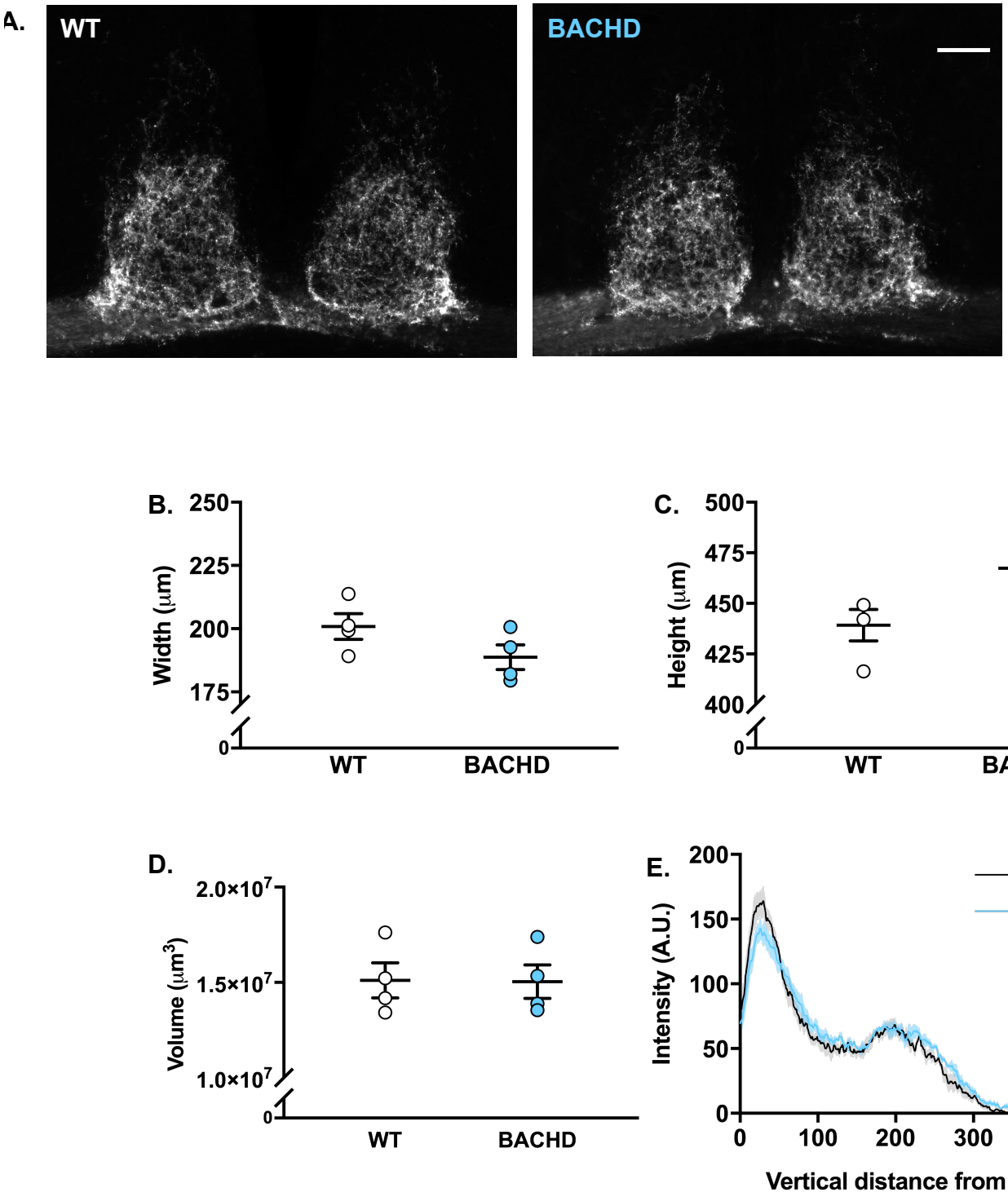
A.
WT
BACHD
B.
Width (μm)
250
225
200
175
0
WT
BACHD
C.
Height (μm)
500
475
450
425
400
0
WT
BACHD
D.
Volume (μm³)
2.0×10⁷
1.5×10⁷
1.0×10⁷
0
WT
BACHD
E.
Intensity (A.U.)
200
150
100
50
0
0
100
200
300
400
500
Vertical distance from OC (μm)
WT
BACHD

Fig. 3: The distribution pattern RHT fibers to the SCN are conserved in BACHD mice. To visualize the RHT input patterns to the SCN, 4mo WT and BACHD mice received bi-lateral intravitreal injections of the anterograde tracer CT-B, which was allowed to travel for 72hrs before tissue collection. **(A)** Group representative images of mid-SCN sections containing RHT fibers. **(B)** Medio-lateral extension measurements (width) of the RHT projections within the SCN of WT and BACHD. **(C)** Ventro-dorsal extension measurements (height) of RHT projections of WT and BACHD. **(D)** Volume measurements of RHT fibers present within the SCN for WT and BACHD. **(E)** Ventro-dorsal density measurements of RHT projections within the SCN from the dorsal limit of the optic chiasm to the dorsal limit of RHT projections. Data are shown as means ± SEM, n=4 animals/genotype, 2 images/animal Scale bar: 100μm.

Fig. 4

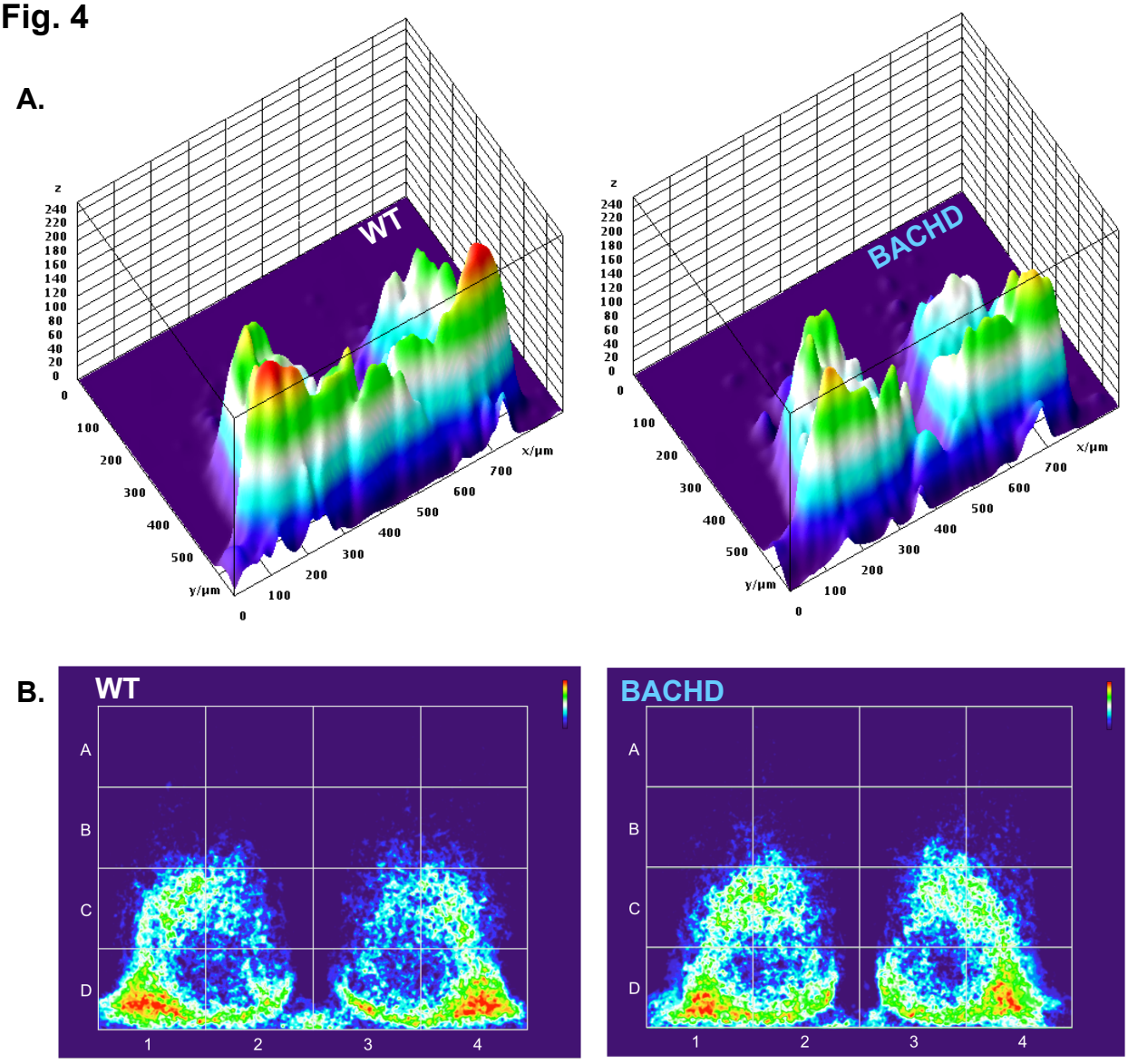

Fig. 4: No changes in the distribution pattern of RHT fibers within the SCN of WT and BACHD mice. Analysis of RHT projections 72 hour after bi-ocular injections of the CT-B anterograde tracer in 4mo WT and BACHD (n=4/genotype). **(A)** Qualitative 3D surface plot of overlaid group binary images for WT and BACHD mice. **(B)** Quantitative heat map of stacked group binary images with ROI overlay (white grid). Heat map color bar shown in upper right. Sum pixel intensity values from heat map ROI analysis are shown in **Table 1**.

WT	1	2	3	4
A	249251±30574	375770±26398	362414±60540	101525±28660
B	215064±20302	686284±50083	640221±123837	91531±24952
C	169233±14348	1312397±35241	1912890±118194	345238±60252
D	101704±16296	876822±80729	1300799±55184	206395±18765

BACHD	1	2	3	4
A	38.3±37.7	120.3±81.7	101±96.8	44.8±53.1
B	1868.3±1288.2	4213±1998.6	6284±2622.3	2416±2378
C	26319.5±5308.1	28527.3±6240.5	27009±10704.6	24395.3±4194
D	48785.8±3381.3	38975.3±7524.7	39039.8±9076	48107±8307.5

Table 1. No changes in the distribution pattern of RHT fibers within the SCN of WT and BACHD mice. Heatmap analysis of the distribution of RHT fibers labeled with CT-B within the demarcated ROI (**Fig.4B**) in the middle SCN of 4mo WT and BACHD mice. Values are the mean ± SEM of the pixels detected in the ROI grid from two consecutive binary images (n=4/genotype). Data was analyzed with a two-tailed *t*-test.

3.3 Photic induction of cFos in WT and BACHD mice.

Upon synaptic release of glutamate and PACAP from terminal RHT fibers, signal transduction cascades are activated in retino-recipient cells within the SCN, which result in the upregulation of multiple gene products including the immediate early gene cFos. In order to assess the integrity of the message transported by the RHT projections to the SCN in BACHD mice, we employed a light-induced cFos experimental paradigm (**Fig. 2A**). In both WT and BACHD, the retino-recipient cells within the SCN exhibited robust cFos induction in response to the light stimulus (**Fig. 5A**). No difference was seen in the number of cFos positive cells (WT: 228 ± 21; BACHD: 235 ± 6; t=0.32, p=0.76), or in the total intensity of the cFos signal in the whole SCN of WT (20.84 ± 3.15) and BACHD (22.97 ± 3.67; t= 0.47, p= 0.65) (**Fig. 5C**) suggesting that the BACHD SCN response to the light is not affected by the mutation. However, we found that the horizonal distribution of cFos staining throughout the SCN was different in WT and BACHD, with the BACHD exhibiting a lower peak of staining intensity in correspondence of the center of the nucleus compared to WT mice, which exhibited a more clustered pattern of cFos expression in the middle of the core (**Fig. 5D**). Upon, vertical distribution analysis we found no differences between WT and BACHD (**Fig.5E**).

Fig. 5

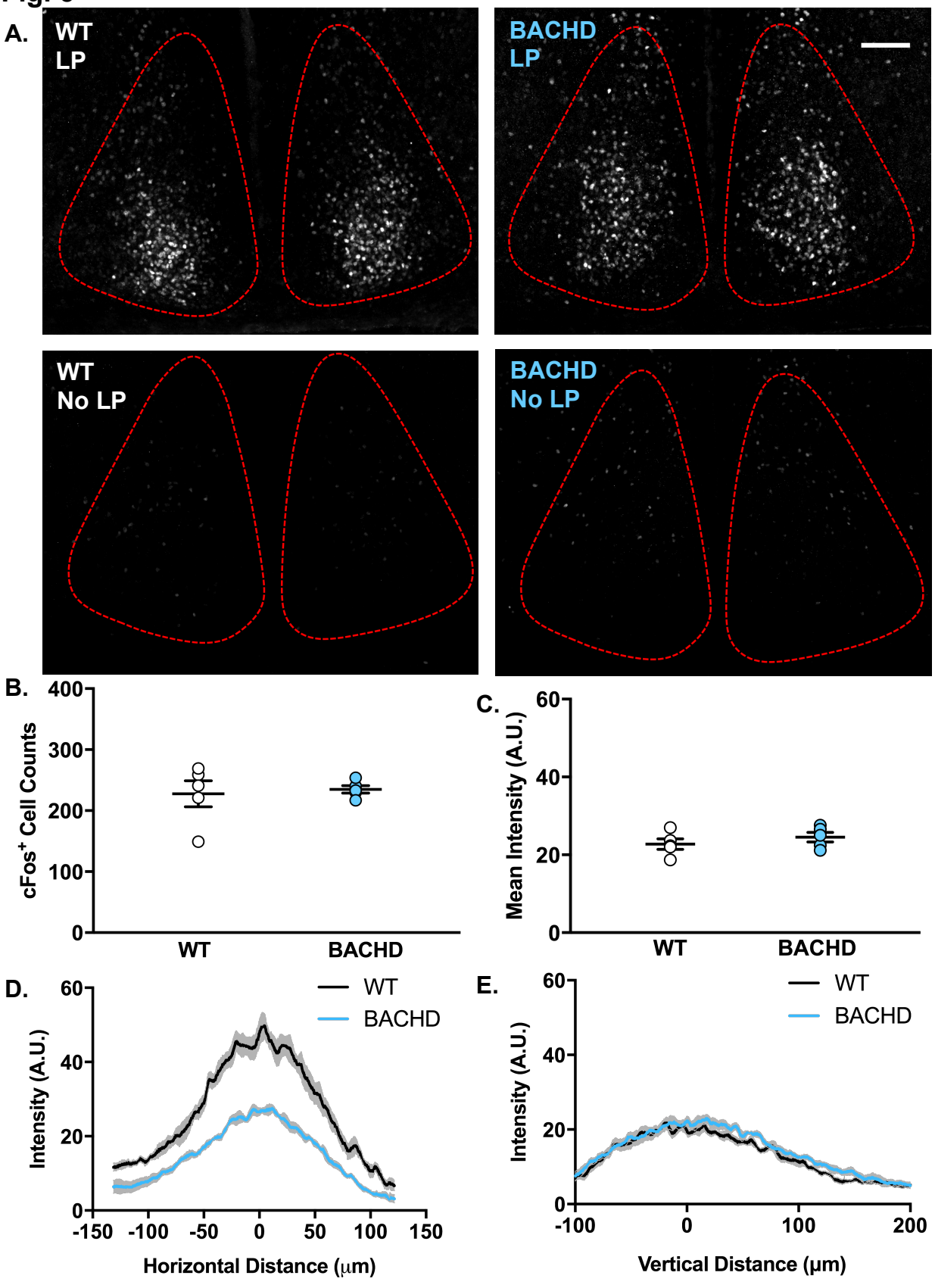
A.
WT
LP
BACHD
LP
WT
No LP
BACHD
No LP
B.
cFos+ Cell Counts
400
300
200
100
0
WT
BACHD
C.
Mean Intensity (A.U.)
60
40
20
0
WT
BACHD
D.
Intensity (A.U.)
60
40
20
0
WT
BACHD
-150
-100
-50
0
50
100
150
Horizontal Distance (μm)
E.
Intensity (A.U.)
60
40
20
0
WT
BACHD
-100
0
100
200
Vertical Distance (μm)

Fig. 5: BACHD mice show differences in the distribution of cFos expression within the SCN. 4mo WT and BACHD mice kept in DD for 3 days, received a light pulse (50lux, 10 min, white light) at CT 16, one hour later animals were perfused and the tissue collected. **(A)** Representative images of cFos immuno-positive cells in the SCN (red dashed line trace) of WT and BACHD mice that received a LP or not (No LP, lower panels). **(B)** Graph showing the number of cFos positive cells in WT and BACHD mice with LP, results are shown as the mean ± SEM of 5 animals/genotype. **(C)** Mean intensity ± SEM of cFos immuno-reactivity in WT and BACHD mice with LP treatment (n=5 animals/genotype). **(D,E)** Horizontal and vertical distribution analysis of cFos immunoreactivty in the SCN of WT and BACHD mice. Scale bar: 100µm.

3.4 Analysis of RHT input to the SCN of Q175 mice.

Next, we examined the RHT input to the SCN in another mouse model of HD, the Q175 mice as shown above for the BACHD model (**Fig. 3A**), Both WT and Q175 mice exhibited the expected characteristic RHT innervation to the SCN, with dense ventro-lateral fibers along while less labeled RHT terminals were seen reaching the central ventral region of SCN (**Fig. 6A**). Quantitative analysis of the RHT projections revealed that Q175 mice exhibited a small reduction (WT: 197±9μm; Q175: 186±7μm; t=0.90, p=0.41) in the labeled fiber in the medio-lateral (width; **Fig. 6B**) as well as a reduction in the fibers extending in a ventro-dorsal (height) manner, from the optic chiasm to the dorsal regions of the SCN (WT: 457±8μm; Q175: 446±12μm; t=0.69, p=0.52) (**Fig. 6C**). Similarly, there was no difference in the volume of RHT fibers present within the SCN in WT ($1.5x10^7$± $3.8x10^5$μm^3) and Q175 mice ($1.5x10^7$±$1.6x10^6$μm^3; t=0.056, p=0.96; **Fig. 6D**). WT and Q175 animals exhibited similar distributions of RHT fibers within the ventral SCN, while, in the dorsal SCN, labeling of the RHT fibers seemed reduced in Q175 mice (**Fig. 6E**). Thus, using binary stacked images overlaid with a ROI grid (**Fig. 1F**), we were able to quantify these differences in distribution patterns between the Q175 and WT mice (**Fig. 7A-B**). Q175 mice exhibited a slight non-significant decrease in the presence of RHT fiber in the dorso-medial (**Table 2**; ROI: 2A, 2B, 3A, 3B) and ventro-medial (**Table 2**; ROI: 2C, 2D, 3C, 3D) regions of the SCN when compared to age matched WT mice. These results suggest that the dorsal SCN of Q175 mice exhibited slight deficits in the distribution of RHT terminals.

Fig. 6

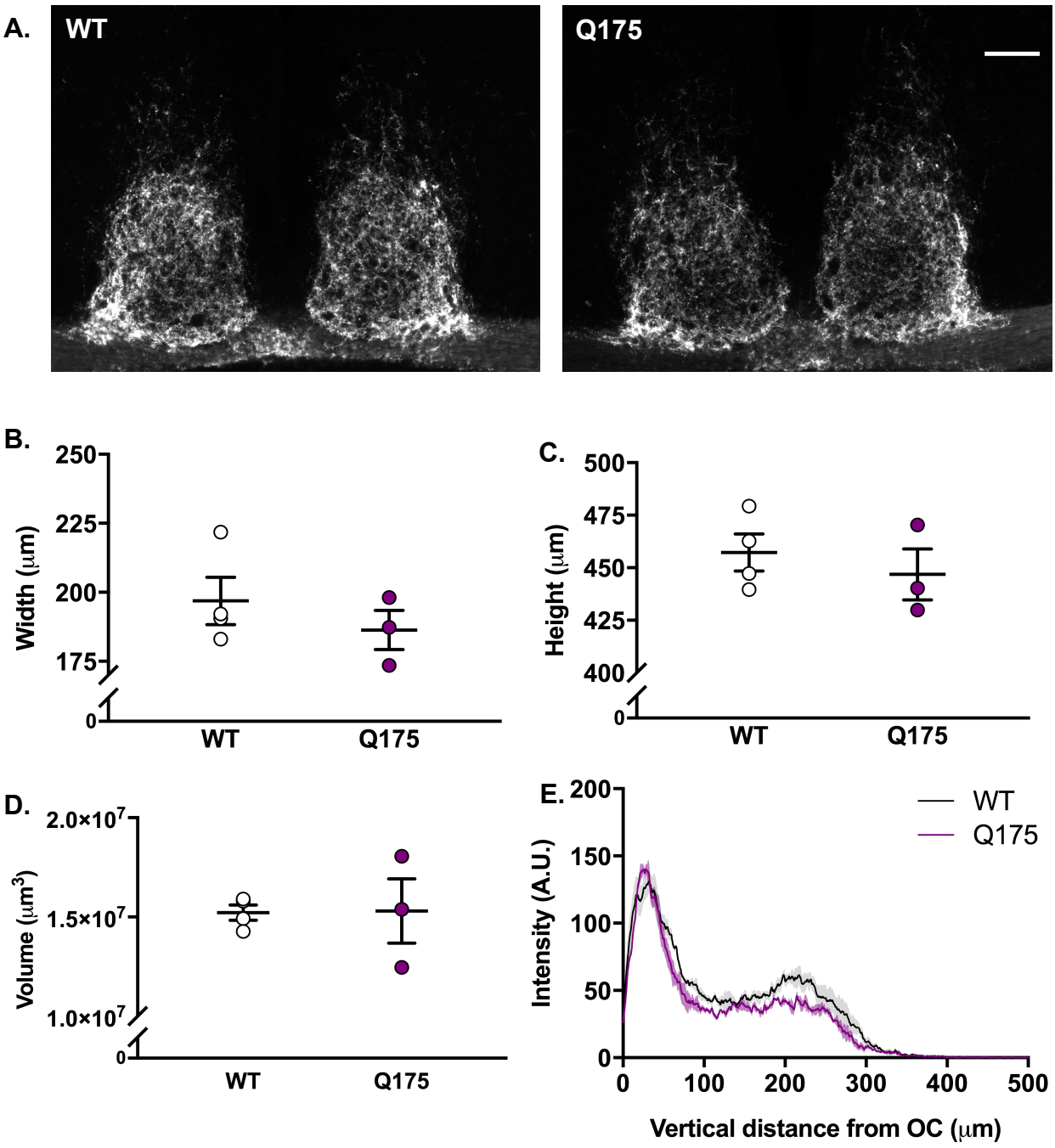
A.
WT
Q175
B.
Width (μm)
250
225
200
175
0
WT
Q175
C.
Height (μm)
500
475
450
425
400
0
WT
Q175
D.
Volume (μm³)
2.0×10⁷
1.5×10⁷
1.0×10⁷
0
WT
Q175
E.
Intensity (A.U.)
200
150
100
50
0
0
100
200
300
400
500
Vertical distance from OC (μm)
WT
Q175

Fig. 6: Q175 mice exhibit slight differences in the amount of RHT terminals within the dorsal SCN. To visualize RHT input patterns in to the SCN, 6mo WT and Q175 mice received a bilateral intravitreal injection of the anterograde tracer CT-B, and their brains were then collected 72hrs later. **(A)** Representative images of RHT fibers into mid-SCN sections. **(B)** Measurements of CB-T labeled RHT projections in the medio-lateral (width) part of the SCN for WT and Q175 mice. **(C)** Measurements of CB-T labeled fibers in the ventro-dorsal part (height) of the SCN in WT and Q175. **(D)** Volume measurements of RHT-labeled fibers within the SCN in WT and Q175 **(E)** Ventro-dorsal distribution measurements of RHT projections within the SCN from the dorsal limit of the optic chiasm to the dorsal limit of RHT projections. Data are shown as mean ± SEM n= 3-4 animals/genotype, Scale bar: 100μm.

Fig. 7

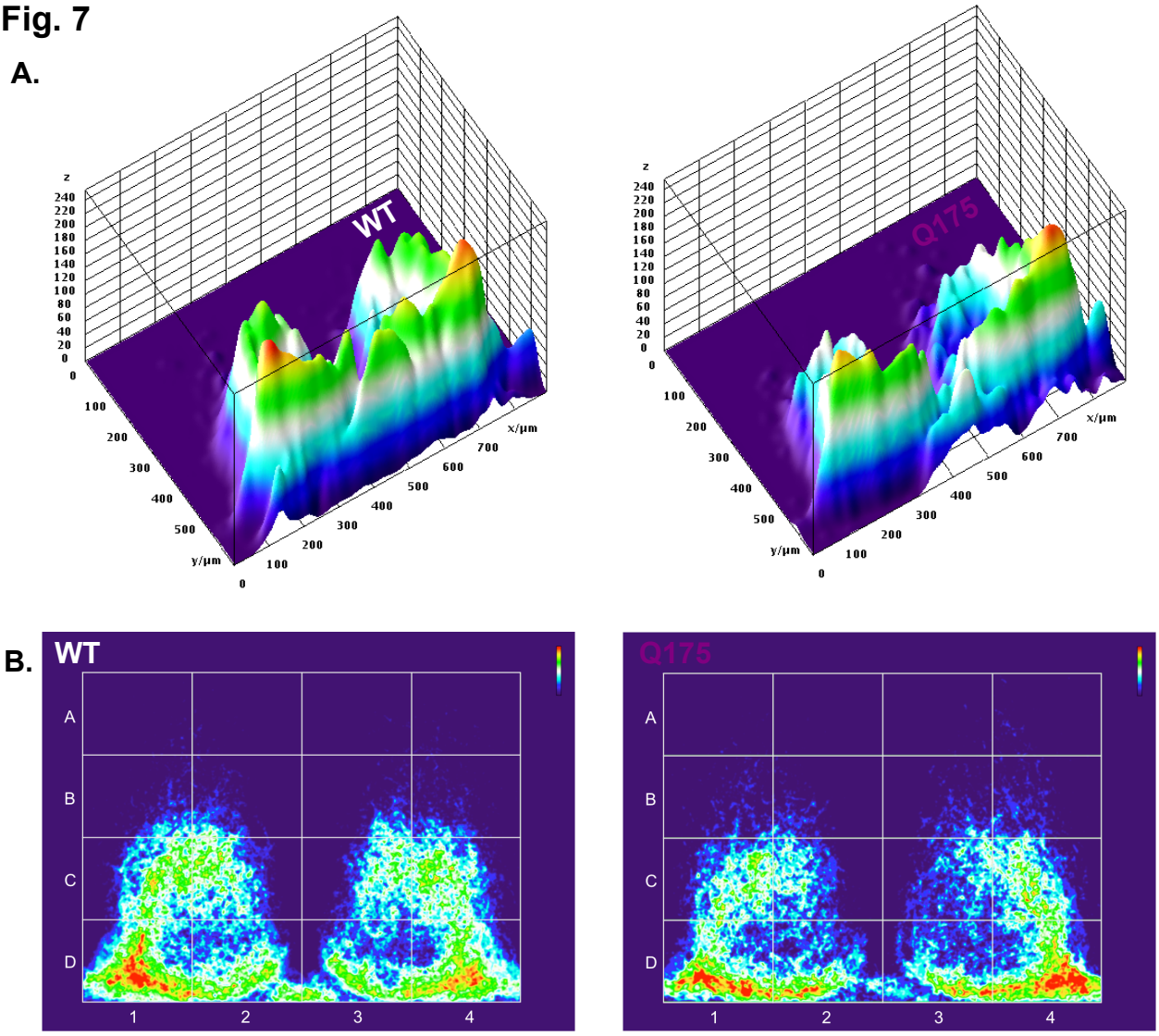

Fig. 7: Q175 mice exhibit slight differences in the distribution of RHT terminal fibers within the dorso-medial SCN. Analysis of RHT projections 72 hour after the bilateral injection of the CT-B anterograde tracer in 6mo WT and Q175 mice. **(A)** Qualitative interactive 3D surface plot of overlaid group binary images containing CT-B fluorescence for WT and Q175 mice. **(B)** Quantitative heat map of stacked group binary images with ROI overlay (white grid). Heat map color bar shown in upper right. Sum of pixel intensity values from heat map ROI analysis are shown in **Table 2.** WT n=4; Q175 n=3.

WT	1	2	3	4
A	206.5 ± 70.3	189.5 ± 49	129.3 ± 50.3	338.3 ± 84
B	6592.5 ± 1223.3	6883.5 ± 1401.8	5749 ± 557.8	5427 ± 689.9
C	41286.3 ± 3284.8	36012.8 ± 3010.6	29244 ± 2854.3	41788 ± 3918.6
D	65119.3 ± 5159.6	49141.3 ± 8503.3	42690 ± 8601.2	61316.5 ± 5828.3

Q175	1	2	3	4
A	146 ± 7.9	45 ± 18.5	132 ± 53.3	511 ± 182.7
B	3668.7 ± 1064	3336 ± 1260.3	4913 ± 2098.7	5672.3 ± 1365.5
C	37420.3 ± 2891.9	22734.7 ± 4619	22523 ± 3566	39749 ± 4815.6
D	58989.7 ± 5539.9	40872 ± 7567.1	38051.3 ± 8891	64922 ± 7610

Table 2: CT-B labeled RHT fiber distribution heatmap analysis within the demarcated ROI (**Fig.7B**) in sections of the middle SCN in 6mo WT (n=4) and Q175 (6 mo, n=3) mice. Values are the mean ± SEM of the pixels detected in the ROI grid of two binary images of the SCN per 3-4 animals/genotype. Data was analyzed with a two-tailed *t*-test.

3.5 Photic induction of cFos in Q175 mice

We utilized the light-induced cFos expression experimental paradigm (**Fig. 1B**) to investigate the responsiveness of retino-recipient cells within the SCN in the Q175 mice. Both WT and Q175 mice exhibited a robust induction of cFos within the SCN (**Fig. 8A**). The number of cFos immuno-positive cells in the SCN was similar in WT (191 ± 35) and Q175 mice (167 ± 36; t= 0.49, p= 0.64) (**Fig. 8B**). Furthermore, the intensity of cFos immuno-reactivity within the whole SCN did not show differences when comparing WT (23.8 ± 5.3) and Q175 mice (19 ± 5.1; t= 0.64, p = 0.55) (**Fig. 8C**). WT and Q175 displayed similar distributions of cFos staining within the SCN (**Fig. 8D,E**).

Fig. 8

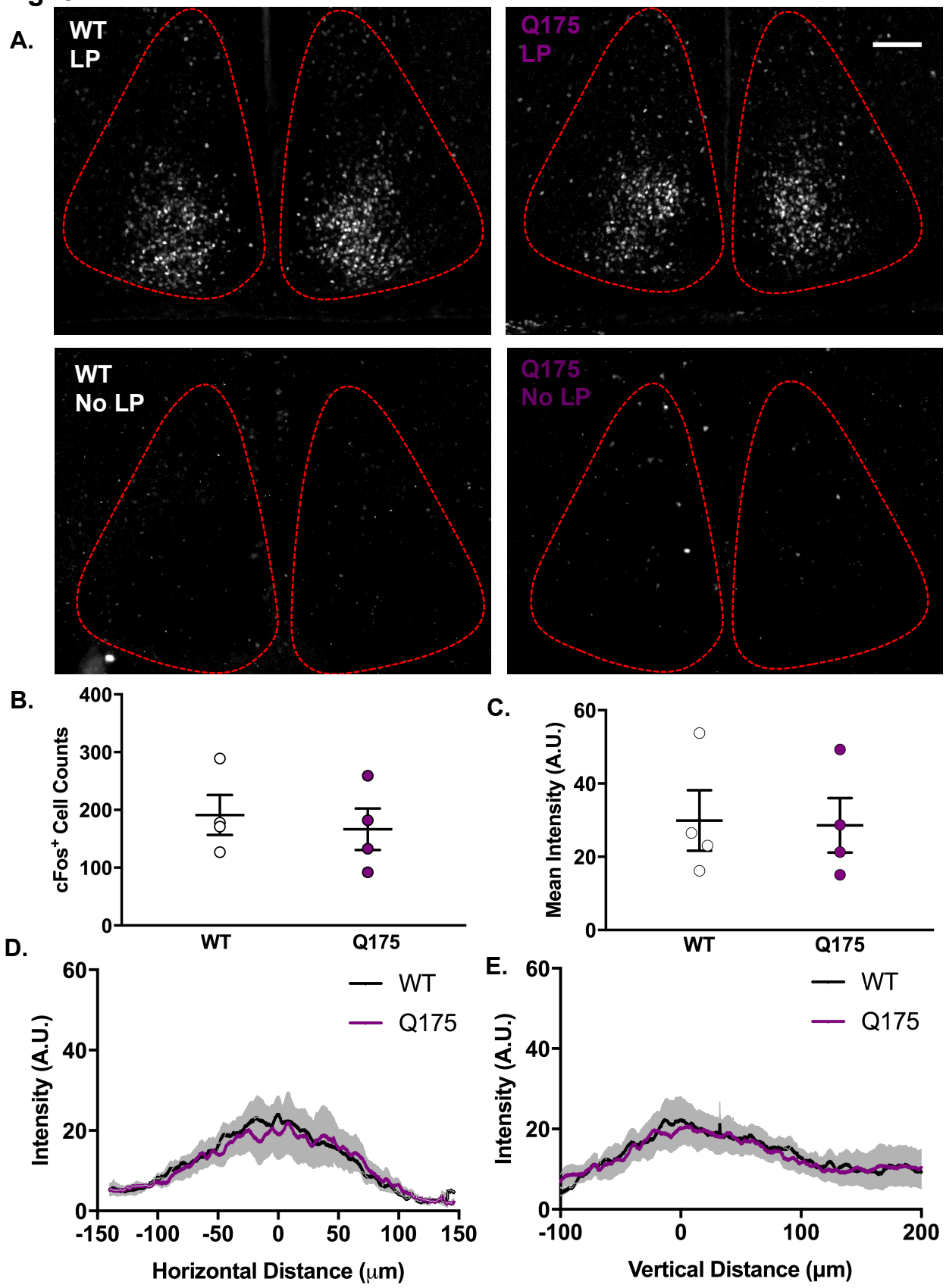
A.
WT
LP
Q175
LP
WT
No LP
Q175
No LP
B.
cFos+ Cell Counts
400
300
200
100
0
WT
Q175
C.
Mean Intensity (A.U.)
60
40
20
0
WT
Q175
D.
Intensity (A.U.)
60
40
20
0
WT
Q175
-150
-100
-50
0
50
100
150
Horizontal Distance (μm)
E.
Intensity (A.U.)
60
40
20
0
WT
Q175
-100
0
100
200
Vertical Distance (μm)

Fig. 8: WT and Q175 mice exhibit similar cFos immunoreactivity within the SCN. 6mo WT and Q175 (6mo, n=4) mice kept in DD for three days received a light pulse (50lux, 10 min, white light) at CT 16. Animals were perfused and the tissue collected one hour after the light pulse. **(A)** Representative images of cFos immuno-reactivity in the SCN (red dashed line trace) of WT and Q175 mice with and without LP. **(B)** immuno-positive cFos cell counts in WT and Q175 mice with LP treatment. **(C)** Mean intensity of cFos immuno-reactivity in WT and Q175 mice with LP treatment. **(D,E)** Horizontal and vertical plot profile analysis of cFos immuno-positive cells with the SCN of WT and Q175 mice, n= 4 animals/genotype. Scale bar: 100µm.

Chapter 4: Is the light input to the SCN intact in a mouse model of Fragile X syndrome?

4.1 Introduction

Disruption in the timing of the sleep-wake cycles is an indication of a possible underlying deregulated circadian system. It is well accepted that light is the most potent zeitgeber and is able to reset rhythms in clock gene expression in central and peripheral oscillators. Deficits in the ability to provide appropriate light information to the SCN may be an underlying cause of circadian dysfunction in disease states. Individuals with neurodevelopmental psychiatric disorders, and related animal models, commonly present with disrupted circadian sleep-wake cycles [76]. Fragile X syndrome (FXS) is a neurodevelopmental disorder that results from genetic silencing of the *FMR1* gene leading to absence of the transcriptional regulator FMRP [70]. FXS patients exhibit disruptions in sleep-wake cycles and melatonin rhythms [77]. Our lab has recently characterized disruptions in rest and activity rhythms in the *Fmr1* KO mouse (Wang et al., in prep). Furthermore, *Fmr1* KO mice exhibit reduced behavioral light response, which implies deficits in the ability to transmit light information to the SCN. Elucidating the presence of any anatomical deficits in the RHT pathway to the master circadian pacemaker in the *Fmr1* KO mouse will provide evidence for a causal link to the observed circadian dysfunctions. Exposing the presence or absence of hampered non-visual light pathways may help establish improved therapeutic strategies for FXS patients and individuals with related disorders.

4.2 Characterization of RHT projections with the SCN of *Fmr1* KO mice

Using established anterograde tract-tracing methods as reported above (**Fig. 1A**), we investigated the presence of abnormalities in RHT projections to the SCN of 4mo WT and *Fmr1* KO mice. WT and *Fmr1* KO mice presented the typical patterns of dense ventro-lateral RHT fiber projections to middle SCN sections, which extend to provide dense fiber presence within the dorsal SCN leaving a characteristic void of dense fibers in the central ventral region of the SCN (**Fig. 9A**). Analysis of the medio-lateral distribution (width; **Fig. 9B**) of CB-T labeled RHT fibers within the ventral SCN showed that *Fmr1* KO mice exhibited a significant reduction when compared to WT mice (WT: 201±5μm; Fmr1 KO: 171±3μm; t=5.03, p=0.0015). However, no differences were found in the ventral extensions (height; WT: 439±8μm; Fmr1KO: 438±7μm; t=0.089, p=0.93, **Fig. 9C**). Interestingly, the total volume of RHT fibers present within the SCN was not affected when comparing the mutant and WT mice (WT: $1.51x10^7$±$9.2x10^5$μm^3; Fmr1KO: $1.48x10^7$±$2.5x10^5$μm^3; t=0.37, p=0.73). In addition, the Fmr1 KO mice exhibited reduced presence of labeled fibers ventrally within 100μm from the optic chiasm and increased dorsal labeling (between 150 and 200 μm from the chiasm) when compared to WT mice (**Fig. 9E**).

To further examine RHT fiber distributions within mid-SCN sections (**Fig. 10A**), we quantified the medio-lateral and ventro-dorsal presence of CT-B labeled fibers using heat maps of stacked binary images with ROI overlay (**Fig. 10B**). WT mice exhibit fibers which were densely present in the ventro-lateral regions of the SCN (**Table 3**: 1D and 4D), while *Fmr1* KO mice showed a greater labeling presence in the dorso-medial

regions of the SCN (**Table 3**: 2C and 3C). These results suggest that the *Fmr1* KO model exhibit subtle deficits in the distribution of terminal RHT fibers within the SCN.

Fig. 9

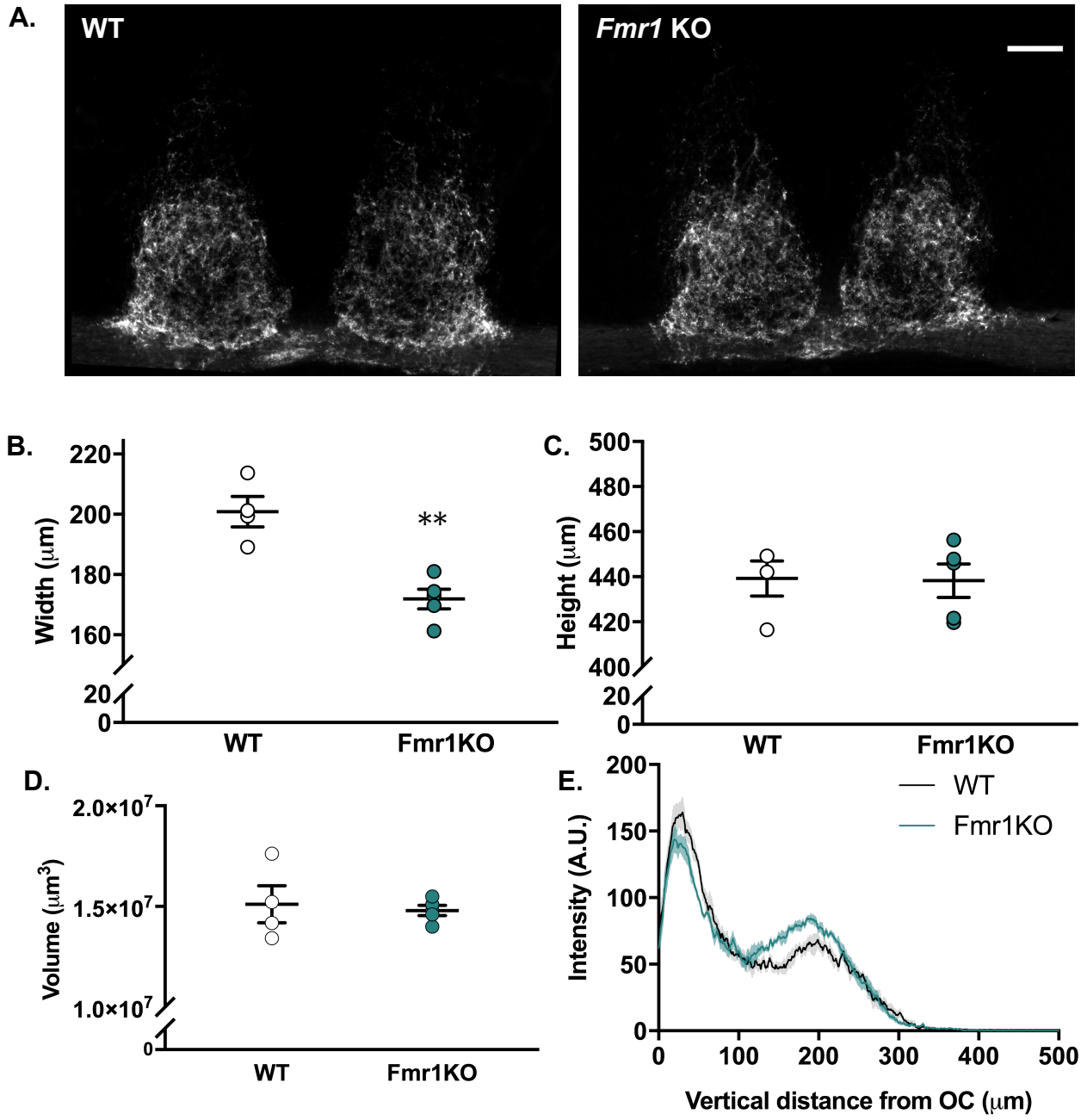
A.
WT
Fmr1 KO
B.
Width (μm)
220
200
180
160
20
0
**
WT
Fmr1KO
C.
Height (μm)
500
480
460
440
420
400
20
0
WT
Fmr1KO
D.
Volume (μm3)
2.0×10^7
1.5×10^7
1.0×10^7
0
WT
Fmr1KO
E.
Intensity (A.U.)
200
150
100
50
0
WT
Fmr1KO
0
100
200
300
400
500
Vertical distance from OC (μm)

Fig. 9: The architectural organization of RHT inputs to the SCN of *Fmr1* KO are disrupted. To visualize RHT input patterns into the SCN, 4mo WT and Fmr1 KO mice received bilateral intravitreal injections of the anterograde tracer CT-B, tissue was collected 72hours later. **(A)** Representative images of RHT inputs to mid-SCN sections. **(B)** Medio-lateral extension (width) measurements of the CB-T labeled RHT projections to the SCN of WT and *Fmr1* KO mice. Data are shown as the mean ± SEM, n= 4-5 mice/genotype. **(C)** Ventro-dorsal extension measurements (height) of RHT projections in WT and *Fmr1* KO. **(D)** Volume measurements of RHT fibers present within the SCN in WT and Q175. **(E)** Ventro-dorsal distribution measurements of RHT projections within the SCN from the dorsal limit of the optic chiasm to the dorsal limit of RHT projections. Data are the mean ± SEM; n=4-5 mice/genotype. Scale bar: 100μm. Double asterisks represent $p = 0.0015$.

Fig. 10

A.

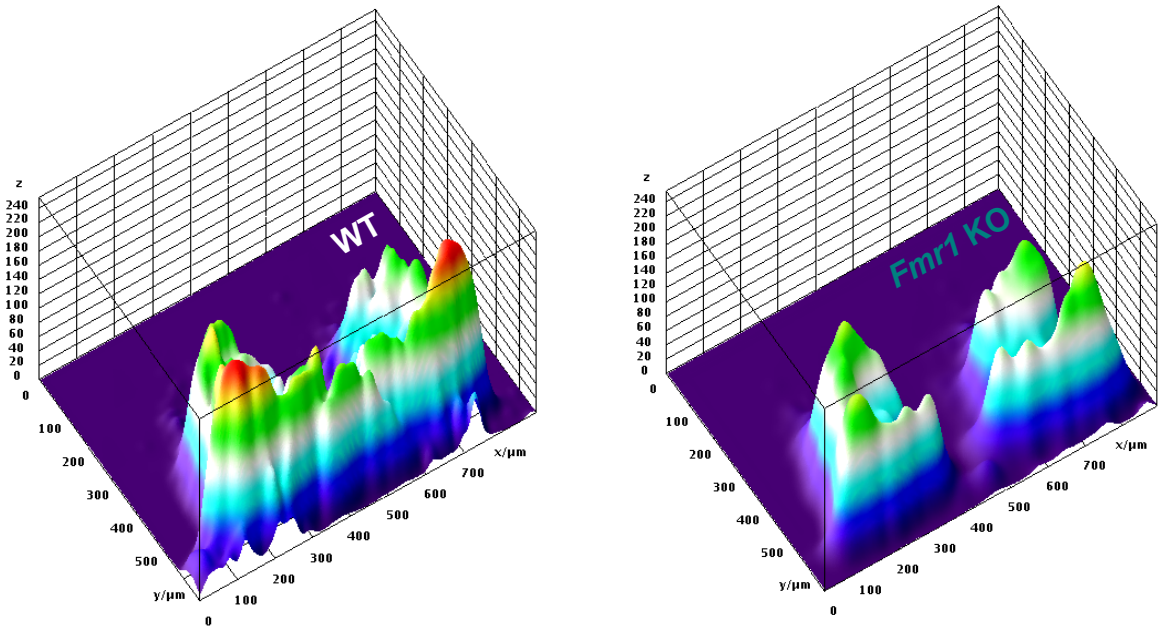

B.

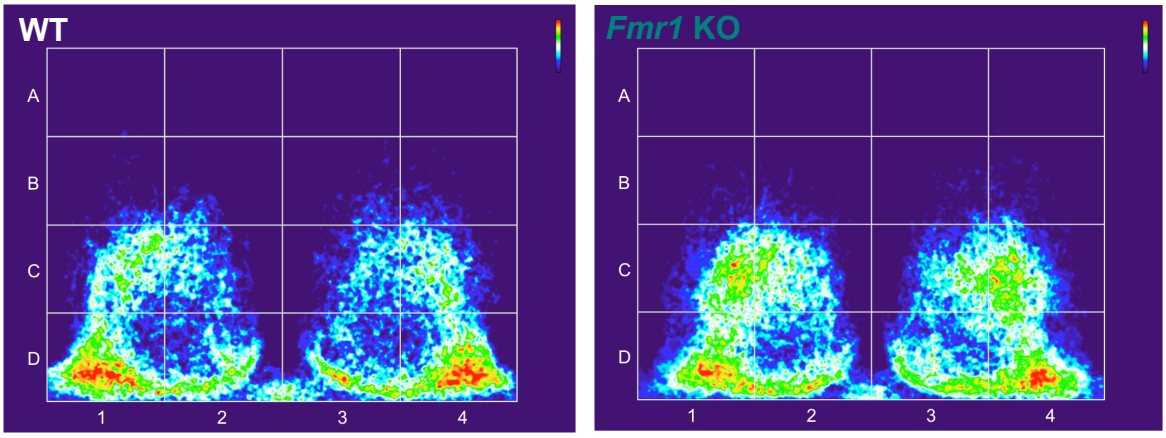

Fig. 10: Distribution patterns of RHT inputs within the SCN are altered in *Fmr1* KO mice. Analysis of CT-B labeled RHT projections. **(A)** Interactive 3D surface plot of overlaid group binary images of WT and Q175 mice. **(B)** Heat map of stacked group binary images with ROI overlay (white grid). Heat map color bar shown in upper right. Mean ± SEM of the sum of the pixel intensity values from heat map ROI analysis are shown in **Table 3**. WT (4 mo, n=4), *Fmr1* KO (4 mo, n=5).

WT	1	2	3	4
A	75±43.3	28.5±13.7	11±1.9	43.5±15.6
B	2482.8±655.4	2962.5±942.7	2739±1334.4	2987.8±1238.7
C	30948±4113.7	19995.3±4719	17532.8±4869.7	27472±2687.1
D	52308.8±4957.2	34209.3±4444.9	32821.8±5556.1	50449.3±2002.4

Fmr1 KO	1	2	3	4
A	20.8±22	23.2±12.3	27.8±26	57.4±45.2
B	1488.6±1347.7	2393.2±1786.3	1631±1276.4	2373.2±1725.7
C	30202.2±10855.1	32595.2±10452.9	26530.6±8078	32680.8±10158
D	47095.4±4907.4	37911±10393.4	39300±10499.8	48713.2±3366.1

Table 3: RHT fiber distribution heatmap analysis of CT-B presence within the demarcated ROI **(Fig.10B**) in sections of the middle SCN of 4mo WT (n=4) and *Fmr1* KO (n=5) mice. Values are presented as the mean ± SEM of the sums of the pixels detected in the ROI grid of binary images. Data was analyzed with a two-tailed *t*-test.

4.3 Photic induction of cFos in *Fmr1* KO mice

Utilizing the light-induced cFos upregulation experimental method (**Fig. 2A**), we explored the responsiveness of retino-recipient cells within the SCN of *Fmr1* KO mice. Both WT and *Fmr1* KO mice demonstrated a robust induction of cFos in response to a light pulse at CT16 (**Fig. 11A**). WT and *Fmr1* KO mice did not show significant difference in the number of cFos positive cells in the SCN (**Fig. 11B**; t=1.26 p = 0.24). Similarly, WT and *Fmr1* KO mice did not show difference in the mean intensity of cFos expression in the SCN (**Fig. 1C**; t=0.92 p = 0.39). Utilizing both horizontal and vertical profile plot analysis, we found that the distribution of cFos positive cells within the *Fmr1* KO SCN was lower and flat, lacking the peak shown by the WT (**Fig. 11D**, **Fig. 11E**). To determine if the distributional differences obtained by profile plot analysis were not purely due to varying levels of cFos expression in retino-recipient cells, we performed ROI (**Fig.2D**) heat map analysis of stacked binary images of the SCN containing cFos immunoreactivity (**Fig. 12A**; **Table 4**). WT mice exhibited a highly structured pattern of cFos expression in the SCN with ventro-lateral regions (**Fig. 12A**; ROI 2C, 3C, 4C, 2D, 3D, 4D,) containing a dense population of cFos positive cells and dorso-medial regions (**Fig. 12A**; ROI 1B, 2B, 3B, 4B, 1C, 1D) containing minimal cFos expression. However, *Fmr1* KO mice exhibited a more dispersed population of cFos positive cells in both the ventro-medial and dorso-lateral regions of the SCN. Upon ROI grid analysis of fluorescent intensity, we found no significant difference in cFos expression in the ventro-medial regions of the SCN between WT and Fmr1KO mice (**Fig. 12C**; WT: $5.95 \times 10^6 \pm 1.29 \times 10^5$; *Fmr1* KO: $5.57 \times 10^6 \pm 2.98 \times 10^5$; t=1.17, p=0.2907). However, we found that *Fmr1* KO mice exhibited a significant increase in cFos expression within the dorsal

lateral regions of the SCN when compared to WT mice (**Fig. 12C**; WT: $1.89x10^6 \pm 1.47x10^5$; *Fmr1* KO: $2.49x10^6 \pm 1.97x10^5$; $t=2.42$, $p=0.0445$). To determine if the observed difference in cFos distribution was due to differences in the architecture of the SCN in WT and *Fmr1* KO mice, we performed a preliminary method of analysis utilizing heat map intensity analysis of DAPI fluorescence on stacked binary images containing the SCN for WT and *Fmr1* KO mice (**Fig. 12B**). While is seems as though WT and *Fmr1* KO SCN exhibited characteristic a pear-like shape, *Fmr1* KO mice may contain a less structured SCN. However, further validation of the method is needed before we can make any stronger claims. Although there is an equivalent amount of light information of reaching the SCN of WT and *Fmr1* KO mice, the organization of retino-recipient cells located in the SCN of *Fmr1* KO mice appears less structured when compared to WT mice.

Fig. 11

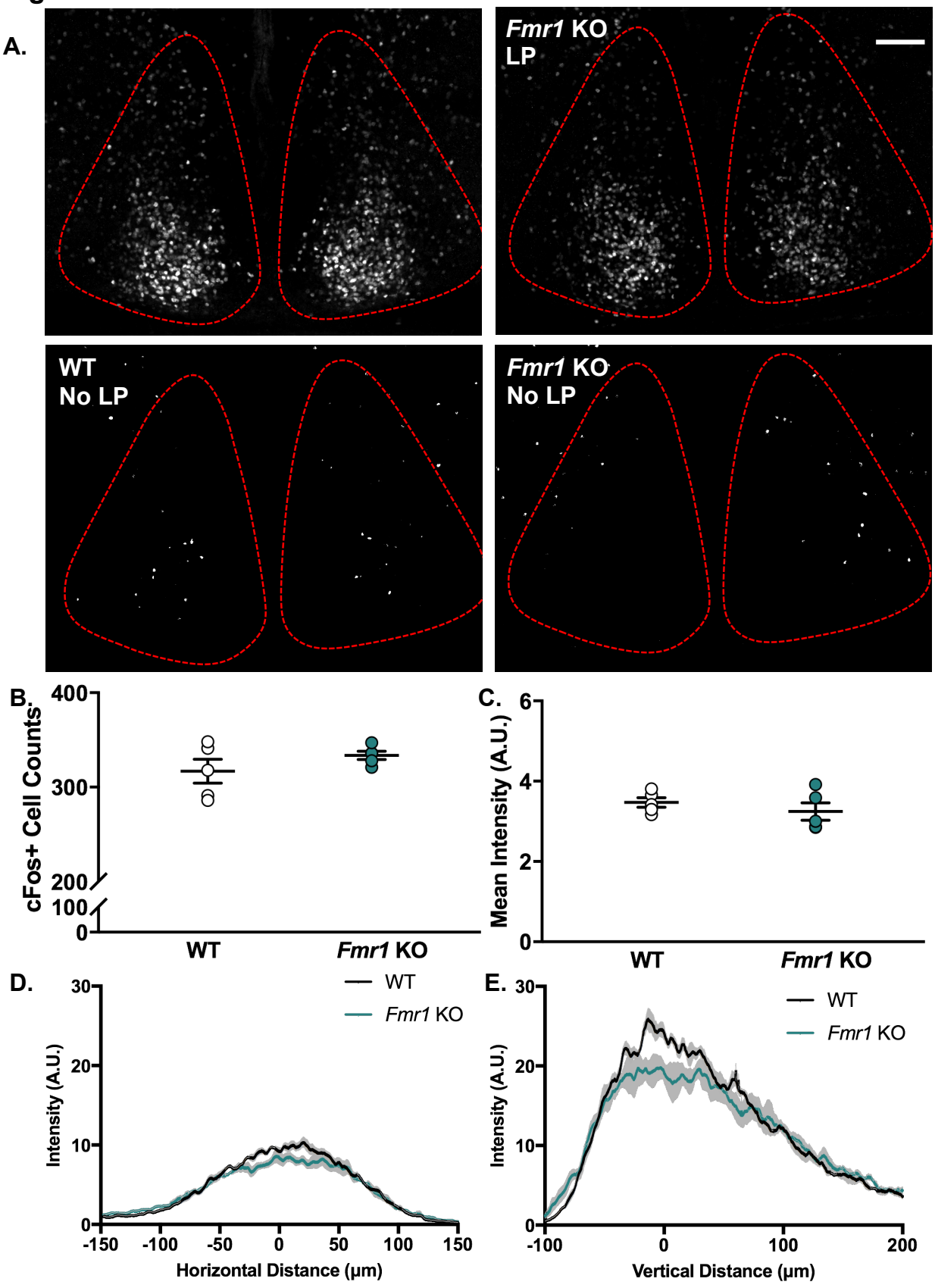
A.
Fmr1 KO
LP
WT
No LP
Fmr1 KO
No LP
B.
cFos+ Cell Counts
400
300
200
100
0
WT
Fmr1 KO
C.
Mean Intensity (A.U.)
6
4
2
0
WT
Fmr1 KO
D.
WT
Fmr1 KO
Intensity (A.U.)
30
20
10
0
-150
-100
-50
0
50
100
150
Horizontal Distance (μm)
E.
WT
Fmr1 KO
Intensity (A.U.)
30
20
10
0
-100
0
100
200
Vertical Distance (μm)

Fig. 11: *Fmr1* KO mice show differences in the distribution of cFos expression within the SCN. After three days of measured activity rhythms in DD, 4 mo WT and *Fmr1* KO mice received a light pulse (50lux, 10 min, white light) at CT 16. Animals were perfused and tissue collected one hour after the start of the light pulse. **(A)** Representative images with and without LP (Lower Panels) cFos immuno-reactivity in the SCN (red dashed line trace) of WT and *Fmr1* KO mice. **(B)** Immuno-positive cFos cell counts in WT and *Fmr1* KO mice with LP treatment. **(C)** Mean intensity of cFos immuno-reactivity in WT and *Fmr1* KO mice with LP treatment. **(D,E)** Horizontal and vertical distribution analysis of cFos imunno-positive cells with the SCN of WT and *Fmr1* KO mice. Values are presented as the mean ± SEM. Scale bar represents 100μm.

Fig. 12

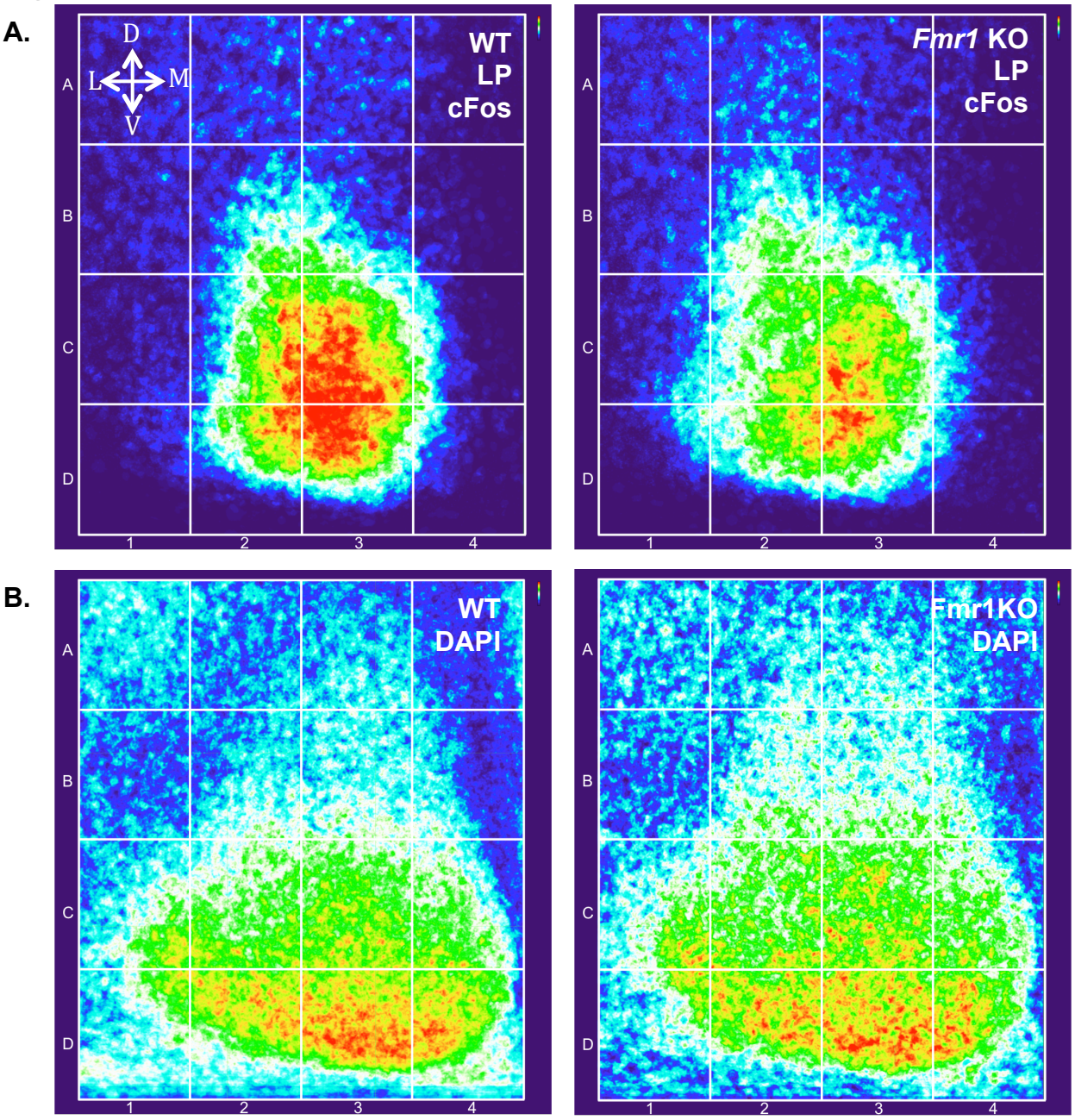
A.
D
L
M
V
WT
LP
cFos
Fmr1 KO
LP
cFos
B.
WT
DAPI
Fmr1KO
DAPI
A
B
C
D
1
2
3
4
C.
8×10^6
6×10^6
4×10^6
2×10^6
0
Intensity (A.U.)
ns
*
WT
Fmr1 KO
Ventro-Medial
Dorso-Lateral

Fig. 12: *Fmr1* KO mice contain altered patterns of cFos expression in the SCN. Analysis of cellular distribution patterns following 10 min light exposure at CT 16. **(A)** Heat map of stacked binary images of the SCN for WT and *Fmr1* KO LP treated animals containing cFos immuno-fluorescence with ROI overlay (white grid). Heat map color bar shown in upper right. Sum of pixel intensity values from heat map ROI analysis are shown in **Table 3**. **(B)** Heat map of stacked binary images of SCN containing DAPI fluorescence with ROI overlay (white grid). **(C)** Sum of cFos pixel intensity present in the ventro-medial regions (C2, C3, C4, D2, D3, D4) and dorso-lateral regions (B1, B2, B3, B4, C1, D1) of the SCN. Values are presented as the mean ± SEM of the sums of the pixels detected in Arbitrary Units (A.U.). WT (4mo, LP n=5), *Fmr1* KO (4mo, LP n=5). Asterisk represents p =0.045

WT (4mo)	1	2	3	4
A	249251±30574	375770±26398	362414±60540	101525±28660
B	215064±20302	686284±50083	640221±123837	91531±24952
C	169233±14348	1312397±35241	1912890±118194	345238±60252
D	101704±16296	876822±80729	1300799±55184	206395±18765

Fmr1 KO (4mo)	1	2	3	4
A	326371±53807	454121±55688	308946±23224	93003±8254
B	299497±46790	925355±66708	616333±65139	92940±21886
C	367538±79626	1409573±168673	1689598±104609	309718±64404
D	195801±36088	930421±79249	1073097±137929	162509±46410

Table 4: Retino-recipient cell distribution heatmap analysis of cFos presence within the demarcated ROI (**Fig.12A**) in sections of the middle SCN for WT (4 mo, n=5) and *Fmr1* KO (4 mo, n=5) mice. Values are presented as the mean sum ± SEM of pixels detected in the ROI grid of binary images containing fluorescence. Data was analyzed with a two-tailed *t*-test.

Chapter 5: Discussion

In this work, we explored the integrity of the RHT projections to the circadian master pacemaker in models of neurodegenerative and neurodevelopmental disease. We found that the light input pathway to the SCN is largely conserved and robust in both models of HD, namely the BACHD and Q175, as well as in the *Fmr1* KO mouse. However, the BACHD and *Fmr1* KO models displayed subtle alterations in the distribution pattern of CB-T labeled RHT projections within the SCN. The BACHD model exhibited reduced RHT projections to the ventral regions of the SCN as well as a dispersed population of cells receiving light information. Similarly, *Fmr1* KO mice contain a significantly altered pattern of RHT input to the SCN together with a more dispersed pattern of cFos immuno-reactivity within the SCN, which offer a possible explanation for some of the behavioral phenotypes observed (Wang et al., in prep).

5.1: The integrity of RHT projections to the SCN of BACHD and Q175 mice is intact and the observed behavioral deficits may be due to an underlying SCN pathology.

Although work from our lab has demonstrated that BACHD mice exhibit reduced behavioral light response as well as attenuated blue-light therapy enhanced recovery compared to Q175 mice [63], both models have light input pathways that are largely maintained. Still, subtle differences in RHT projections to the SCN are present in both models. The ventral region of the SCN receives a majority of the retinal input and contains a dense population of VIP cells and the dorsal SCN contains a dense population of AVP cells and receives less retinal input [21]. We found that Q175 mice have reduced organization of RHT terminal fibers in the dorsal SCN and no difference

RHT fiber densities in the ventral SCN. However, the Q175 mice did not show a difference in the distribution of light responsive cells within the SCN. In contrast, we found that BACHD mice have reduced ventral RHT fiber densities and no difference in dorsal retinal projections. The BACHD mice also exhibit characteristics of dispersed light responsive cells within the SCN. These results confirm that sufficient light information is reaching the SCN of the HD mouse models and suggests that the previously observed reduced behavioral light response in the BACHD model maybe due to the potential SCN pathology of these mice.

The progression of HD results in increased immune cell activation as well as cell loss within the SCN [78-79]. We have evidence that HD also affects glial cell functions, and found that both astrocytes and microglial cells are increased in male BACHD striatum, corpus callosum and motor cortex as early as 3mo (Cheung, Whittaker et al., unpublished results). Although previous work from our lab has demonstrated that BACHD mice do not exhibit changes in VIP or AVP cell population in the SCN at 3mo [60], we cannot rule out the potential loss or altered function of other neuronal and glial cell types within the SCN. Astrocytes are the most abundant cells in the brain and their ability to regulate synaptic communications in several brain areas, including the SCN, has been widely investigated and described [80-82]. Astrocytes express several ionic channels and, among others, both ionotropic and metabotropic glutamate receptors which resemble the neuronal counterpart. In the absence of neurotransmitter signaling, complex networks of astrocytes exhibit spontaneous rhythms in increased intracellular calcium ($[CA^{2+}]_i$) [83]. In response to increases in $[CA^{2+}]_i$, astrocytes demonstrate astrocyte-astrocyte as well as astrocyte-neuron intercellular communication through the

release of gliotransmitters such as glutamate, purines, GABA, and D-serine [84]. Astrocytes also respond to glutamate release with $[CA^{2+}]_i$ [85], and calcium waves, which are able to propagate quite a distance, triggering response in other parts of a brain region [86], [87]. The ability of astrocytes to respond to light information reaching the SCN is illustrated by their expression of cFos in response to light exposure [46]. In mice, specific ablation of *Bmal1* in this glia subtype resulted in an increased period of rhythms in SCN electrical activity as well as locomotor activity [81], [82]. RHT projections synapsing with retino-recipient cells within the SCN are glutamatergic. Astrocytes possess the ability to regulate extracellular glutamate through the unique glutamate transporters EAAT1/2 at the synapse between RHT efferent projections and retino-recipient cells [88], [89]. Thus, mutant HTT in SCN astrocytes could alter their ability to respond to and regulate the light-induced glutamate release, contributing to the observed altered response. Astrocytes have the ability to alter normal cellular function and contribute to disease progression [90]. Implantation of human glial progenitor cells (hGPCs) transfected with mHTT into the striatum of WT mice, which persisted as progenitors or became astrocytes produced HD characterized motor deficits as well as hyperexcitability in striatal neurons compared to animals implanted with hGPCs containing vector control [90]. Transplantation of normal hGPCs into transgenic R6/2 HD mice, restored some aspects of altered electrophysiological and behavioral functions. Results from this study warrant the investigation of dysfunctional astrocytes in the SCN of BACHD mice.

5.2: The integrity of RHT projections to the SCN of *Fmr1* KO mice is intact and the observed behavioral deficits may be due to an underlying SCN pathology.

We found that the integrity of the RHT input to the SCN of *Fmr1* KO mice is preserved. However, *Fmr1* KO mice do exhibit significantly altered distributions of RHT projections as well as light responsive cell populations within the SCN. RHT projections within the SCN of *Fmr1* KO mice are reduced in ventral regions as well as increased in the dorsal regions. These results implicate the observed behavioral deficits in light responsiveness is not due to a hampered ability of the RHT to relay light information but an underlying pathology present in the SCN. Although the teardrop shape of the SCN may be conserved in the *Fmr1* KO mouse, our preliminary results suggest that the SCN of these mice may have an altered organization of retino-recipient cells within the SCN and a dispersed cellular phenotype in the dorsal regions of the SCN. Intriguingly, the SCN's ability to generate rhythms in electrical activity and chemical output is derived from the aggregate coupling of each autonomous single cell circadian oscillator present within it [18]. Therefore, the observed dispersed retino-recipient cell populations within the SCN may dampen the ability of the SCN to coordinate sufficient output and subsequent behavioral response.

However, the reduced ability of *Fmr1* KO mice to respond behaviorally to light may also be a result of altered biochemical and cellular pathways in the mutants. FMRP is a RNA binding protein that regulates the local translation of a subset of mRNAs at neuronal synapses acting in response to mGluR activation, thus its loss results in altered synaptic function and protein synthesis dependent plasticity [71]. Similarly, conditional knock out of FMRP in cortical astrocyte leads to a reduction in the astrocyte

specific glutamate transporter 1, EAAT2 [91], which when appropriately functioning has the potential to regulate extracellular glutamate. Furthermore, it is has been shown that the SCN undergoes rhythmic ultrastructural rearrangements over the 24hr cycle, which is characterized by day/night changes in astrocytic -axon terminal and/or -somato-dendritic coverage of neurons expressing VIP and AVP [92]. VIP cells within the SCN exhibit increased synaptic coverage by astrocytes during the dark/active phase and reduced coverage in the light/rest phase. Brain-derived neurotropic factor (BDNF) signaling through its receptor, tropomyosin receptor kinase B (TrkB), regulates these daily ultrastructural rearrangements of the neuronal-glial network present in the SCN [93]. Pharmacological blockade of TrkB abolishes these rhythms in synaptic coverage resulting in increased coverage of VIP cells within the SCN around the clock. Interestingly in WT animals, the expression FMRP is negatively regulated by BDNF/ TrkB [94]. Increased BDNF/TrkB signaling results in reduced expression of FMRP. Therefore, the absence of FMRP in *Fmr1* KO mice may directly alter the ability of astrocytes to regulate glutamate at the RHT synapse with retino-recipient cells within the SCN, which could contribute to the SCN pathology resulting in the observed behavioral deficits in response to light during their active phase.

5.3: Conclusions and future directions

Symptoms of circadian dysfunction are comorbid with both neurodegenerative and neurodevelopmental disease states. Deficits in the ability of light information to reach the SCN may provide a mechanistic explanation of how the presence of a deregulated circadian system may exacerbate some of the symptoms of these

diseases. Our study investigated the presence of deficits in the light input pathway to the SCN in HD and FXS mouse models. We found that the ability of light information to reach the SCN is not altered in these models providing further justification for the use of light therapy in neurodegenerative and neurodevelopmental diseases. Importantly, our results suggest that the behavioral deficits observed in response to a light pulse in BACHD and *Fmr1* KO mice are likely the product of a dysfunctional SCN circuit. Future investigation of the pathology present in the SCN of these mice may provide insight to the presented circadian dysfunction as well as to mechanisms of disease progression.

References

[1] J. S. Takahashi, "Transcriptional architecture of the mammalian circadian clock," *Nat. Rev. Genet.*, vol. 18, no. 3, pp. 164–179, Mar. 2017.

[2] D. C. Klein, R. Y. Moore, and S. M. Reppert, *Suprachiasmatic Nucleus: The Mind's Clock*. Oxford University Press, 1991.

[3] C. S. Colwell, "Linking neural activity and molecular oscillations in the SCN," *Nat. Rev. Neurosci.*, vol. 12, no. 10, pp. 553–569, Oct. 2011.

[4] C. Lee, J. P. Etchegaray, F. R. Cagampang, A. S. Loudon, and S. M. Reppert, "Posttranslational mechanisms regulate the mammalian circadian clock," *Cell*, vol. 107, no. 7, pp. 855–867, Dec. 2001.

[5] N. Preitner *et al.*, "The orphan nuclear receptor REV-ERBalpha controls circadian transcription within the positive limb of the mammalian circadian oscillator," *Cell*, vol. 110, no. 2, pp. 251–260, Jul. 2002.

[6] T. K. Sato *et al.*, "A functional genomics strategy reveals Rora as a component of the mammalian circadian clock," *Neuron*, vol. 43, no. 4, pp. 527–537, Aug. 2004.

[7] S. M. Reppert and D. R. Weaver, "Coordination of circadian timing in mammals," *Nature*, vol. 418, no. 6901, pp. 935–941, Aug. 2002.

[8] U. Schibler and P. Sassone-Corsi, "A web of circadian pacemakers," *Cell*, vol. 111, no. 7, pp. 919–922, Dec. 2002.

[9] T. J. Bartness, C. K. Song, and G. E. Demas, "SCN efferents to peripheral tissues: implications for biological rhythms," *J. Biol. Rhythms*, vol. 16, no. 3, pp. 196–204, Jun. 2001.

[10] C. B. Saper, "The central circadian timing system," *Curr. Opin. Neurobiol.*, vol. 23, no. 5, pp. 747–751, Oct. 2013.

[11] R. Y. Moore and V. B. Eichler, "Loss of a circadian adrenal corticosterone rhythm following suprachiasmatic lesions in the rat," *Brain Res.*, vol. 42, no. 1, pp. 201–206, Jul. 1972.

[12] F. K. Stephan and I. Zucker, "Circadian Rhythms in Drinking Behavior and Locomotor Activity of Rats Are Eliminated by Hypothalamic Lesions," *Proc. Natl. Acad. Sci. U. S. A.*, vol. 69, no. 6, pp. 1583–1586, Jun. 1972.

[13] M. N. Lehman, R. Silver, W. R. Gladstone, R. M. Kahn, M. Gibson, and E. L. Bittman, "Circadian rhythmicity restored by neural transplant. Immunocytochemical

characterization of the graft and its integration with the host brain," *J. Neurosci. Off. J. Soc. Neurosci.*, vol. 7, no. 6, pp. 1626–1638, Jun. 1987.

[14] M. R. Ralph, R. G. Foster, F. C. Davis, and M. Menaker, "Transplanted suprachiasmatic nucleus determines circadian period," *Science*, vol. 247, no. 4945, pp. 975–978, Feb. 1990.

[15] S. T. Inouye and H. Kawamura, "Persistence of circadian rhythmicity in a mammalian hypothalamic 'island' containing the suprachiasmatic nucleus.," *Proc. Natl. Acad. Sci. U. S. A.*, vol. 76, no. 11, pp. 5962–5966, Nov. 1979.

[16] S. J. Aton, C. S. Colwell, A. J. Harmar, J. Waschek, and E. D. Herzog, "Vasoactive intestinal polypeptide mediates circadian rhythmicity and synchrony in mammalian clock neurons," *Nat. Neurosci.*, vol. 8, no. 4, pp. 476–483, Apr. 2005.

[17] A. B. Webb, N. Angelo, J. E. Huettner, and E. D. Herzog, "Intrinsic, nondeterministic circadian rhythm generation in identified mammalian neurons," *Proc. Natl. Acad. Sci. U. S. A.*, vol. 106, no. 38, pp. 16493–16498, Sep. 2009.

[18] C. Liu, D. R. Weaver, S. H. Strogatz, and S. M. Reppert, "Cellular Construction of a Circadian Clock: Period Determination in the Suprachiasmatic Nuclei," *Cell*, vol. 91, no. 6, pp. 855–860, Dec. 1997.

[19] E. E. Abrahamson and R. Y. Moore, "Suprachiasmatic nucleus in the mouse: retinal innervation, intrinsic organization and efferent projections," *Brain Res.*, vol. 916, no. 1–2, pp. 172–191, Oct. 2001.

[20] T. Hamada, M. C. Antle, and R. Silver, "Temporal and spatial expression patterns of canonical clock genes and clock-controlled genes in the suprachiasmatic nucleus," *Eur. J. Neurosci.*, vol. 19, no. 7, pp. 1741–1748, Apr. 2004.

[21] R. K. Leak and R. Y. Moore, "Topographic organization of suprachiasmatic nucleus projection neurons," *J. Comp. Neurol.*, vol. 433, no. 3, pp. 312–334, May 2001.

[22] T. Kalamatianos, I. Kalló, H. D. Piggins, and C. W. Coen, "Expression of VIP and/or PACAP receptor mRNA in peptide synthesizing cells within the suprachiasmatic nucleus of the rat and in its efferent target sites," *J. Comp. Neurol.*, vol. 475, no. 1, pp. 19–35, Jul. 2004.

[23] I. N. Karatsoreos, L. Yan, J. LeSauter, and R. Silver, "Phenotype Matters: Identification of Light-Responsive Cells in the Mouse Suprachiasmatic Nucleus," *J. Neurosci.*, vol. 24, no. 1, pp. 68–75, Jan. 2004.

[24] J.-D. Li *et al.*, "Attenuated Circadian Rhythms in Mice Lacking the Prokineticin 2 Gene," *J. Neurosci. Off. J. Soc. Neurosci.*, vol. 26, no. 45, pp. 11615–11623, Nov. 2006.

[25] J. Lu *et al.*, "Contrasting effects of ibotenate lesions of the paraventricular nucleus and subparaventricular zone on sleep-wake cycle and temperature regulation," *J. Neurosci. Off. J. Soc. Neurosci.*, vol. 21, no. 13, pp. 4864–4874, Jul. 2001.

[26] N. Vujovic, J. J. Gooley, T. C. Jhou, and C. B. Saper, "Projections from the subparaventricular zone define four channels of output from the circadian timing system," *J. Comp. Neurol.*, vol. 523, no. 18, pp. 2714–2737, Dec. 2015.

[27] M. S. Freedman *et al.*, "Regulation of mammalian circadian behavior by non-rod, non-cone, ocular photoreceptors," *Science*, vol. 284, no. 5413, pp. 502–504, Apr. 1999.

[28] A. Terakita, "The opsins," *Genome Biol.*, vol. 6, no. 3, p. 213, 2005.

[29] R. J. Lucas, R. H. Douglas, and R. G. Foster, "Characterization of an ocular photopigment capable of driving pupillary constriction in mice," *Nat. Neurosci.*, vol. 4, no. 6, pp. 621–626, Jun. 2001.

[30] I. Provencio, I. R. Rodriguez, G. Jiang, W. P. Hayes, E. F. Moreira, and M. D. Rollag, "A novel human opsin in the inner retina," *J. Neurosci. Off. J. Soc. Neurosci.*, vol. 20, no. 2, pp. 600–605, Jan. 2000.

[31] D. M. Graham, K. Y. Wong, P. Shapiro, C. Frederick, K. Pattabiraman, and D. M. Berson, "Melanopsin ganglion cells use a membrane-associated rhabdomeric phototransduction cascade," *J. Neurophysiol.*, vol. 99, no. 5, pp. 2522–2532, May 2008.

[32] M. T. Walker, R. L. Brown, T. W. Cronin, and P. R. Robinson, "Photochemistry of retinal chromophore in mouse melanopsin," *Proc. Natl. Acad. Sci. U. S. A.*, vol. 105, no. 26, pp. 8861–8865, Jul. 2008.

[33] W. Sperling and C. N. Rafferty, "Relationship between Absorption Spectrum and Molecular Conformations of 11-cis-Retinal," *Nature*, vol. 224, no. 5219, p. 224591a0, Nov. 1969.

[34] S. S. Pires *et al.*, "Differential expression of two distinct functional isoforms of melanopsin (Opn4) in the mammalian retina," *J. Neurosci. Off. J. Soc. Neurosci.*, vol. 29, no. 39, pp. 12332–12342, Sep. 2009.

[35] A. Jagannath *et al.*, "Isoforms of Melanopsin Mediate Different Behavioral Responses to Light," *Curr. Biol. CB*, vol. 25, no. 18, pp. 2430–2434, Sep. 2015.

[36] D. M. Berson, F. A. Dunn, and M. Takao, "Phototransduction by retinal ganglion cells that set the circadian clock," *Science*, vol. 295, no. 5557, pp. 1070–1073, Feb. 2002.

[37] S. Panda *et al.*, "Melanopsin (Opn4) requirement for normal light-induced circadian phase shifting," *Science*, vol. 298, no. 5601, pp. 2213–2216, Dec. 2002.

[38] Q. Cui, C. Ren, P. J. Sollars, G. E. Pickard, and K.-F. So, "THE INJURY RESISTANT ABILITY OF MELANOPSIN-EXPRESSING INTRINSICALLY PHOTOSENSITIVE RETINAL GANGLION CELLS," *Neuroscience*, vol. 284, pp. 845–853, Jan. 2015.

[39] S. B. Baver, G. E. Pickard, P. J. Sollars, and G. E. Pickard, "Two types of melanopsin retinal ganglion cell differentially innervate the hypothalamic suprachiasmatic nucleus and the olivary pretectal nucleus," *Eur. J. Neurosci.*, vol. 27, no. 7, pp. 1763–1770, Apr. 2008.

[40] M. A. Belenky, C. A. Smeraski, I. Provencio, P. J. Sollars, and G. E. Pickard, "Melanopsin retinal ganglion cells receive bipolar and amacrine cell synapses," *J. Comp. Neurol.*, vol. 460, no. 3, pp. 380–393, Jun. 2003.

[41] T. J. Viney *et al.*, "Local retinal circuits of melanopsin-containing ganglion cells identified by transsynaptic viral tracing," *Curr. Biol. CB*, vol. 17, no. 11, pp. 981–988, Jun. 2007.

[42] T. M. Schmidt and P. Kofuji, "Differential cone pathway influence on intrinsically photosensitive retinal ganglion cell subtypes," *J. Neurosci. Off. J. Soc. Neurosci.*, vol. 30, no. 48, pp. 16262–16271, Dec. 2010.

[43] T. M. Schmidt and P. Kofuji, "Structure and function of bistratified intrinsically photosensitive retinal ganglion cells in the mouse," *J. Comp. Neurol.*, vol. 519, no. 8, pp. 1492–1504, Jun. 2011.

[44] J. Hannibal, "Neurotransmitters of the retino-hypothalamic tract," *Cell Tissue Res.*, vol. 309, no. 1, pp. 73–88, Jul. 2002.

[45] D. C. Fernandez, Y.-T. Chang, S. Hattar, and S.-K. Chen, "Architecture of retinal projections to the central circadian pacemaker," *Proc. Natl. Acad. Sci.*, vol. 113, no. 21, pp. 6047–6052, May 2016.

[46] M. R. Bennett and W. J. Schwartz, "Are glia among the cells that express immunoreactive c-Fos in the suprachiasmatic nucleus?," *Neuroreport*, vol. 5, no. 14, pp. 1737–1740, Sep. 1994.

[47] L. P. Morin and C. N. Allen, "The circadian visual system, 2005," *Brain Res. Rev.*, vol. 51, no. 1, pp. 1–60, Jun. 2006.

[48] C. La Morgia, F. N. Ross-Cisneros, A. A. Sadun, and V. Carelli, "Retinal Ganglion Cells and Circadian Rhythms in Alzheimer's Disease, Parkinson's Disease, and Beyond," *Front. Neurol.*, vol. 8, p. 162, 2017.

[49] T. J. Nakamura *et al.*, "Age-Related Changes in the Circadian System Unmasked by Constant Conditions(1,2,3)," *eNeuro*, vol. 2, no. 4, Aug. 2015.

[50] G. Esquiva, P. Lax, J. J. Pérez-Santonja, J. M. García-Fernández, and N. Cuenca, "Loss of Melanopsin-Expressing Ganglion Cell Subtypes and Dendritic Degeneration in the Aging Human Retina," *Front. Aging Neurosci.*, vol. 9, p. 79, 2017.

[51] C. La Morgia *et al.*, "Melanopsin retinal ganglion cells and circadian dysfunction in Alzheimer´s disease," *Acta Ophthalmol. (Copenh.)*, vol. 91, pp. 0–0, Aug. 2013.

[52] C. La Morgia *et al.*, "Melanopsin retinal ganglion cell loss in Alzheimer disease," *Ann. Neurol.*, vol. 79, no. 1, pp. 90–109, Jan. 2016.

[53] J.-Y. Lee, J. Ahn, T. W. Kim, and B. S. Jeon, "Optical coherence tomography in Parkinson's disease: is the retina a biomarker?," *J. Park. Dis.*, vol. 4, no. 2, pp. 197–204, 2014.

[54] K. Ouk, S. Hughes, C. A. Pothecary, S. N. Peirson, and A. Jennifer Morton, "Attenuated pupillary light responses and downregulation of opsin expression parallel decline in circadian disruption in two different mouse models of Huntington's disease," *Hum. Mol. Genet.*, vol. 25, no. 24, 27 2016.

[55] A. Ciammola *et al.*, "Increased apoptosis, Huntingtin inclusions and altered differentiation in muscle cell cultures from Huntington's disease subjects," *Cell Death Differ.*, vol. 13, no. 12, pp. 2068–2078, Dec. 2006.

[56] C. Saft *et al.*, "Mitochondrial impairment in patients and asymptomatic mutation carriers of Huntington's disease," *Mov. Disord. Off. J. Mov. Disord. Soc.*, vol. 20, no. 6, pp. 674–679, Jun. 2005.

[57] K. Duff *et al.*, "Mild cognitive impairment in prediagnosed Huntington disease," *Neurology*, vol. 75, no. 6, pp. 500–507, Aug. 2010.

[58] J. Marshall *et al.*, "Specific psychiatric manifestations among preclinical Huntington disease mutation carriers," *Arch. Neurol.*, vol. 64, no. 1, pp. 116–121, Jan. 2007.

[59] M. Orth *et al.*, "Observing Huntington's disease: the European Huntington's Disease Network's REGISTRY," *J. Neurol. Neurosurg. Psychiatry*, vol. 82, no. 12, pp. 1409–1412, Dec. 2011.

[60] T. Kudo *et al.*, "Dysfunctions in circadian behavior and physiology in mouse models of Huntington's disease," *Exp. Neurol.*, vol. 228, no. 1, pp. 80–90, Mar. 2011.

[61] D. A. Kuljis *et al.*, "Sex Differences in Circadian Dysfunction in the BACHD Mouse Model of Huntington's Disease," *PloS One*, vol. 11, no. 2, p. e0147583, 2016.

[62] D. H. Loh, T. Kudo, D. Truong, Y. Wu, and C. S. Colwell, "The Q175 mouse model of Huntington's disease shows gene dosage- and age-related decline in circadian rhythms of activity and sleep," *PloS One*, vol. 8, no. 7, p. e69993, 2013.

[63] H.-B. Wang *et al.*, "Blue light therapy improves circadian dysfunction as well as motor symptoms in two mouse models of Huntington's disease," *Neurobiol. Sleep Circadian Rhythms*, vol. 2, pp. 39–52, Jan. 2017.

[64] D. A. Regier, E. A. Kuhl, and D. J. Kupfer, "The DSM-5: Classification and criteria changes," *World Psychiatry Off. J. World Psychiatr. Assoc. WPA*, vol. 12, no. 2, pp. 92–98, Jun. 2013.

[65] G. Glickman, "Circadian rhythms and sleep in children with autism," *Neurosci. Biobehav. Rev.*, vol. 34, no. 5, pp. 755–768, Apr. 2010.

[66] S. Kotagal and E. Broomall, "Sleep in children with autism spectrum disorder," *Pediatr. Neurol.*, vol. 47, no. 4, pp. 242–251, Oct. 2012.

[67] S. Tordjman *et al.*, "Altered circadian patterns of salivary cortisol in low-functioning children and adolescents with autism," *Psychoneuroendocrinology*, vol. 50, pp. 227–245, Dec. 2014.

[68] M. Martyn *et al.*, "Offering fragile X syndrome carrier screening: a prospective mixed-methods observational study comparing carrier screening of pregnant and non-pregnant women in the general population," *BMJ Open*, vol. 3, no. 9, p. e003660, Sep. 2013.

[69] D. C. Crawford, J. M. Acuña, and S. L. Sherman, "FMR1 and the fragile X syndrome: human genome epidemiology review," *Genet. Med. Off. J. Am. Coll. Med. Genet.*, vol. 3, no. 5, pp. 359–371, Oct. 2001.

[70] A. J. Verkerk *et al.*, "Identification of a gene (FMR-1) containing a CGG repeat coincident with a breakpoint cluster region exhibiting length variation in fragile X syndrome," *Cell*, vol. 65, no. 5, pp. 905–914, May 1991.

[71] G. J. Bassell and S. T. Warren, "Fragile X syndrome: loss of local mRNA regulation alters synaptic development and function," *Neuron*, vol. 60, no. 2, pp. 201–214, Oct. 2008.

[72] M. Bernardet and W. E. Crusio, "Fmr1 KO mice as a possible model of autistic features," *ScientificWorldJournal*, vol. 6, pp. 1164–1176, Sep. 2006.

[73] "Fmr1 knockout mice: a model to study fragile X mental retardation. The Dutch-Belgian Fragile X Consortium," *Cell*, vol. 78, no. 1, pp. 23–33, Jul. 1994.

[74] N. A. Aziz, G. V. Anguelova, J. Marinus, G. J. Lammers, and R. A. C. Roos, "Sleep and circadian rhythm alterations correlate with depression and cognitive impairment in Huntington's disease," *Parkinsonism Relat. Disord.*, vol. 16, no. 5, pp. 345–350, Jun. 2010.

[75] A. J. Morton, N. I. Wood, M. H. Hastings, C. Hurelbrink, R. A. Barker, and E. S. Maywood, "Disintegration of the sleep-wake cycle and circadian timing in Huntington's disease," *J. Neurosci. Off. J. Soc. Neurosci.*, vol. 25, no. 1, pp. 157–163, Jan. 2005.

[76] I. N. Karatsoreos, "Links between Circadian Rhythms and Psychiatric Disease," *Front. Behav. Neurosci.*, vol. 8, May 2014.

[77] E. L. Gould, D. Z. Loesch, M. J. Martin, R. J. Hagerman, S. M. Armstrong, and R. M. Huggins, "Melatonin profiles and sleep characteristics in boys with fragile X syndrome: a preliminary study," *Am. J. Med. Genet.*, vol. 95, no. 4, pp. 307–315, Dec. 2000.

[78] M. Björkqvist *et al.*, "A novel pathogenic pathway of immune activation detectable before clinical onset in Huntington's disease," *J. Exp. Med.*, vol. 205, no. 8, pp. 1869–1877, Aug. 2008.

[79] D. J. van Wamelen *et al.*, "Suprachiasmatic Nucleus Neuropeptide Expression in Patients with Huntington's Disease," *Sleep*, vol. 36, no. 1, pp. 117–125, Jan. 2013.

[80] G. Perea, M. Navarrete, and A. Araque, "Tripartite synapses: astrocytes process and control synaptic information," *Trends Neurosci.*, vol. 32, no. 8, pp. 421–431, Aug. 2009.

[81] M. Brancaccio, A. P. Patton, J. E. Chesham, E. S. Maywood, and M. H. Hastings, "Astrocytes Control Circadian Timekeeping in the Suprachiasmatic Nucleus via Glutamatergic Signaling," *Neuron*, vol. 93, no. 6, p. 1420–1435.e5, Mar. 2017.

[82] C. F. Tso, T. Simon, A. C. Greenlaw, T. Puri, M. Mieda, and E. D. Herzog, "Astrocytes Regulate Daily Rhythms in the Suprachiasmatic Nucleus and Behavior," *Curr. Biol. CB*, vol. 27, no. 7, pp. 1055–1061, Apr. 2017.

[83] F. Aguado, J. F. Espinosa-Parrilla, M. A. Carmona, and E. Soriano, "Neuronal activity regulates correlated network properties of spontaneous calcium transients in astrocytes in situ," *J. Neurosci. Off. J. Soc. Neurosci.*, vol. 22, no. 21, pp. 9430–9444, Nov. 2002.

[84] M. V. Sofroniew and H. V. Vinters, "Astrocytes: biology and pathology," *Acta Neuropathol. (Berl.)*, vol. 119, no. 1, pp. 7–35, Jan. 2010.

[85] J. T. Porter and K. D. Mccarthy, "ASTROCYTIC NEUROTRANSMITTER RECEPTORS IN SITU AND IN VIVO," *Prog. Neurobiol.*, vol. 51, no. 4, pp. 439–455, Mar. 1997.

[86] A. Verkhratsky and F. Kirchhoff, "Glutamate-mediated neuronal–glial transmission," *J. Anat.*, vol. 210, no. 6, pp. 651–660, Jun. 2007.

[87] M. M. Halassa and P. G. Haydon, "Integrated Brain Circuits: Astrocytic Networks Modulate Neuronal Activity and Behavior," *Annu. Rev. Physiol.*, vol. 72, no. 1, pp. 335–355, Mar. 2010.

[88] C. M. Anderson and R. A. Swanson, “Astrocyte glutamate transport: review of properties, regulation, and physiological functions,” *Glia*, vol. 32, no. 1, pp. 1–14, Oct. 2000.

[89] S. H. Oliet, R. Piet, and D. A. Poulain, “Control of glutamate clearance and synaptic efficacy by glial coverage of neurons,” *Science*, vol. 292, no. 5518, pp. 923–926, May 2001.

[90] A. Benraiss *et al.*, “Human glia can both induce and rescue aspects of disease phenotype in Huntington disease,” *Nat. Commun.*, vol. 7, p. ncomms11758, Jun. 2016.

[91] H. Higashimori *et al.*, “Selective Deletion of Astroglial FMRP Dysregulates Glutamate Transporter GLT1 and Contributes to Fragile X Syndrome Phenotypes In Vivo,” *J. Neurosci. Off. J. Soc. Neurosci.*, vol. 36, no. 27, pp. 7079–7094, Jul. 2016.

[92] D. Becquet, C. Girardet, F. Guillaumond, A.-M. François-Bellan, and O. Bosler, “Ultrastructural plasticity in the rat suprachiasmatic nucleus. Possible involvement in clock entrainment,” *Glia*, vol. 56, no. 3, pp. 294–305, Feb. 2008.

[93] C. Girardet *et al.*, “Brain-derived neurotrophic factor/TrkB signaling regulates daily astroglial plasticity in the suprachiasmatic nucleus: electron-microscopic evidence in mouse,” *Glia*, vol. 61, no. 7, pp. 1172–1177, Jul. 2013.

[94] M. Castrén *et al.*, “BDNF regulates the expression of fragile X mental retardation protein mRNA in the hippocampus,” *Neurobiol. Dis.*, vol. 11, no. 1, pp. 221–229, Oct. 2002.